



Droplet distributions at the liquid core of a turbulent spray

Sam S. Yoon

Citation: [Physics of Fluids \(1994-present\)](#) **17**, 035103 (2005); doi: 10.1063/1.1852577

View online: <http://dx.doi.org/10.1063/1.1852577>

View Table of Contents: <http://scitation.aip.org/content/aip/journal/pof2/17/3?ver=pdfcov>

Published by the [AIP Publishing](#)



Re-register for Table of Content Alerts

Create a profile.



Sign up today!



Droplet distributions at the liquid core of a turbulent spray

Sam S. Yoon^{a)}

Fire Science and Technologies, Sandia National Laboratories, P.O. Box 5800, Albuquerque, New Mexico 87185-1135

(Received 28 April 2004; accepted 19 November 2004; published online 28 January 2005)

Initial droplet distributions at the liquid core are examined for various Weber number and pulsing conditions. While experimental investigation in the liquid core region is nearly impossible due to difficulty in the optical access to the region, the distribution at the region is investigated computationally, and typical droplet distributions are identified. It is found that the Nukiyama–Tanasawa and log-normal distributions can best describe the droplet size and velocity distributions, respectively. By comparing computational results obtained at the liquid core ($0 < x < 8$ mm) and experimental data collected at $x = 48$ mm, it is suspected that the droplet gradation occurs immediately after droplets are separated from the liquid core. Thus, the distribution shape changes rapidly in both axial and radial directions. Such droplet–gradation behavior is numerically confirmed when the Nukiyama–Tanasawa droplet size distribution is used as an initial condition for the stochastic separated flow model. When the jet velocity is increased, the width of the droplet-size distribution becomes narrower, while the droplet velocity distribution becomes broader. Possible physical mechanism for that behavior is discussed in detail. Pulsing injection prominently influences the external spray shape near the nozzle exit. However, the overall droplet size and velocity distributions of the liquid core due to the pulsing injection are relatively insignificant for a turbulent spray in the atomization regime. © 2005 American Institute of Physics.

[DOI: 10.1063/1.1852577]

I. INTRODUCTION

To conduct liquid spray simulations, it is necessary to provide an appropriate initial droplet-size distribution characterization. Since the distribution at the liquid core is generally unknown, one typically chooses a certain distribution function (i.e., Gaussian, log-normal, Rosin–Rammler, and Nukiyama–Tanasawa, etc.) for the initial condition and estimates the required parameters. While this approach to prescribing the initial conditions is common, it is well known that simulations are sensitive to the selected initial conditions. For example, smaller droplets tend to transfer mass, momentum, and heat to the surrounding gas more rapidly, and a distribution that overestimates the number of small droplets is more likely to overestimate initial transfer rates. Naturally, an overestimate of the number of large droplets would have the opposite effect. A similar series of consequences would hold if droplet–droplet collision were significant: The droplet number per unit mass is much greater given a distribution weighted towards larger droplets, and this would result in substantially more droplet collisions. Because droplet evolution depends strongly on the droplet size, the size distribution plays an important role in providing optimum operating conditions for numerous industrial applications (i.e., inkjet printer, agricultural sprays, internal-combustion engine, and fire suppression, etc.).

Among the existing distribution functions, the Rosin–Rammler and the log-normal distributions are used frequently because of their simple mathematical expressions

with parameters easily adjusted to fit the experimental data. More complicated distribution functions (such as Nukiyama–Tanasawa and log-hyperbolic) are known to fit the experimental data more effectively^{1–4} because these distribution functions have more degrees of freedom controlling the distribution shape, as more adjustable constants are involved. All of these distribution shapes are realistically asymmetric, allowing matching of some widely known experimental data.⁵

Predicting droplet sizes in liquid jets has been of great interest to the atomization community because of the aforementioned importance. Numerous linear theories^{6–11} have achieved notable success predicting the dominant instability wavelengths and, thus, the arithmetic mean diameter. Generally, these linear theories work well for low-velocity laminar jets. For high-velocity turbulent jets, the linear theories often are empirically reformulated to predict the most accurate droplet size. However, these empirical extrapolation techniques require relevant experimental data. In addition, measurements are thus far limited to the optically accessible region somewhat downstream of the liquid core. Measurements within the liquid core of a turbulent spray are nearly impossible because optical access is obscured. Some authors^{12–16} attempted to model the initial droplet distribution using the maximum entropy principle (MEP). Their newly formulated distributions were applied to spray simulators [i.e., KIVA (Ref. 17)], and their computational results were in good agreement with experimental data at a certain downstream location. It should be warned that one should not underestimate the consequence of some flow physics (which we will prove and demonstrate in this paper) imme-

^{a)}Author to whom correspondence should be addressed. Telephone: 505-284-8400. Fax: 505-845-3151. Electronic mail: ssyoon@sandia.gov

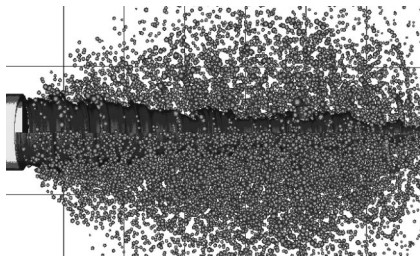


FIG. 1. Liquid core simulation by Park, Yoon, and Heister (Ref. 25). Courtesy of Park *et al.* (Ref. 25).

diately after droplets are pinched-off and separated from the liquid slug (or core); droplet distribution may change from the nozzle exit to a certain downstream location. Since the authors^{12–16} had not truly investigated nor compared the droplet distribution at the liquid core, their newly developed distribution functions had not been truly validated and, therefore, the size distribution using the MEP is applicable only in a certain downstream location. We attempt to remove these uncertainties in the previous work^{12–16} by “directly” simulating the production of the droplet size and velocity at the liquid core; no empirically based scaling constant is used to predict droplet characteristics.

In the present work, we employ the computational methods of Yoon and Heister¹⁸ to directly predict the droplet size and velocity distributions resulting from the initial liquid core breakup. The computational method also provides surface structures of the spray liquid core, while its shape is still unknown despite the current effort of using the state-of-the-art x-ray technique.^{19–24} The capability of the computational method is briefly demonstrated in Fig. 1. Results of these predictions are compared with measurements a short distance downstream of the initial breakup to identify the flow physics after the droplet separation from the liquid core. The differences indicate key physics occurring in the initial development of the spray. The predicted droplet size distributions also are compared with the typically selected presumed-shape droplet distributions. Variation of the droplet size distribution with Weber number and the effects of periodic forcing of the initial liquid jet also are examined. In this paper, we attempt to identify and characterize droplet distributions (in both size and velocity) associated with the liquid core breakup. The resulting probability density functions (PDF) of the droplet size and velocity are examined at various Weber numbers. The role of periodic disturbances in the liquid core flow also is examined. Computational results are compared with extrapolated experimental data of Yoon *et al.*² Once these initial PDFs of the liquid core are identified, we apply the initial conditions to a Lagrangian droplet tracking model to observe the behavior of the droplet dynamics over the computational domain. Several important characteristics of the droplet launching mechanism, as well as external spray flow physics, are identified.

II. MODELING THE LIQUID CORE BREAKUP

Evolution of the liquid jet is simulated from the point when the liquid leaves a cylindrical pipe through develop-

ment of instabilities, the breakup of liquid elements into axisymmetric rings, and finally into individual droplets. A boundary-element-method (BEM) is described in this section to model the liquid evolution through the point when individual rings of liquid separate from the central liquid core. Modeling of the secondary breakup is described in the following section.

Reference 18 provides a complete description of the model regarding the liquid core breakup; in the interest of brevity, only highlights are presented. Formulation of the BEM starts with the integral representation of Laplace’s equation, $\nabla^2\phi=0$, with ϕ being the velocity potential under an assumption that fluids are inviscid and incompressible. Following Liggett and Liu,²⁶ the integral equation for this Laplace equation is

$$\alpha\phi(\vec{r}_i) + \int_S \left[\phi \frac{\partial G}{\partial \hat{n}} - qG \right] ds = 0, \quad (1)$$

where $\phi(\vec{r}_i)$ is the value of the potential at a point \vec{r}_i , S is the boundary of the two-dimensional (2D) domain, α is the singularity contribution of the boundary point, and G is the free space Green’s function corresponding to Laplace’s equation. Linear elements are assumed for the velocity potential, ϕ , and its normal velocity, $q = \partial\phi/\partial n$. Jet injection velocity (U), the orifice radius (a), and liquid density (ρ) are used as non-dimensional parameters.

The unsteady Bernoulli equation is used as the boundary condition along a free-surface interface as follows:

$$\frac{\partial\phi}{\partial t} + \frac{1}{2} |\nabla\phi_t|^2 + P_g + \frac{\kappa}{We} - \frac{Bo}{We} z = 0, \quad (2)$$

where ϕ_t represents the total value for ϕ , P_g is the gas pressure, κ is the curvature of the free surface, and the Weber and Bond numbers are

$$We = \frac{\rho U^2 a}{\sigma}, \quad Bo = \frac{\rho g a^2}{\sigma}. \quad (3)$$

A more general solution can be obtained through the principle of superposition for potential flow. Since the Laplacian governing equation is linear, we may superimpose the potential flow with the potential vortex ring as shown in Fig. 2. Thus,

$$\phi_t = \phi + \phi_v. \quad (4)$$

Since the differential operator is a linear function, the superposition theory holds for the velocity as well. Thus,

$$u_t = u + u_v, \quad v_t = v + v_v, \quad (5)$$

where $u = \partial\phi/\partial z$ and $v = \partial\phi/\partial r$. An analytical solution for the vortex ring-induced velocities, $(\)_v$, is available.¹⁸ Applying the Reynolds transport theorem to Eq. (2) and combining the theory of superposition gives the following nonlinear boundary condition for the free surface:

$$\frac{D\phi}{Dt} = \frac{1}{2} |\vec{u}_t|^2 - \vec{u}_t \cdot \vec{u}_v - P_g - \frac{\kappa}{We} + \frac{Bo}{We} z. \quad (6)$$

Due to the nature of elliptical partial differential equation, a matrix of the governing equation in Eq. (1) is fully dense,

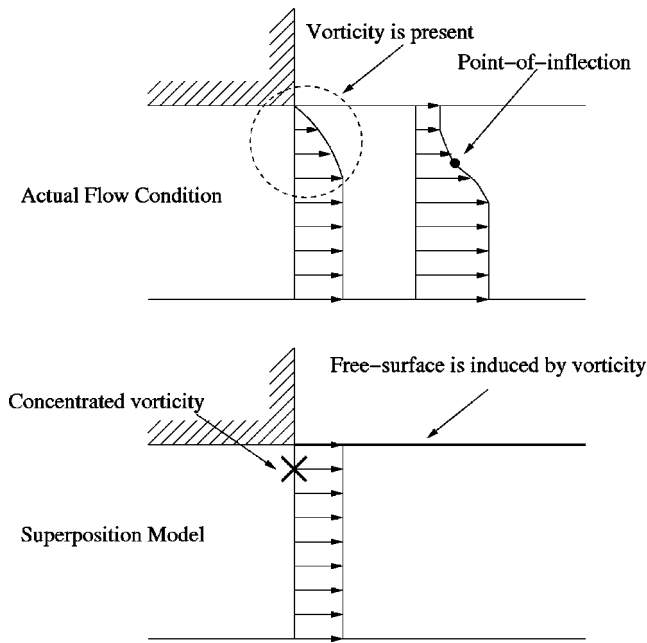


FIG. 2. Comparing the actual physical flow condition with the superposition model simulating boundary layer relaxation downstream of the orifice's exit plane.

and, thus, the computational cost is timely expensive. In addition, simulation of the growing jet requires continuously implementing the computational node on the liquid surface. For these reasons, a parallel matrix solver is utilized.

III. INITIAL CONDITIONS AT THE NOZZLE EXIT

The BEM simulations begin at the exit plane of a nozzle. It is assumed that turbulent pipe flow exists in the nozzle approaching the exit plane. The boundary-layer circulation associated with this flow is imposed on the BEM simulation in the form of discrete vortex rings of a circulation corresponding to the boundary layer as indicated in Fig. 2.

A. Vortex ring location

The vortex ring is located radially at the vorticity centroid determined as follows. Assuming a power-law turbulent velocity profile,²⁷ the velocity profile can be expressed as

$$u^*(r^*) = (1 - r^*)^{1/n}, \quad (7)$$

where $u^* = u/U$, U is the center-line velocity, $r^* = r/a$, and r is an axis starting from the center line ($r=0$) to the wall ($r=a$). The centroid definition (i.e., $\bar{r}^* = \int_0^1 r^* du^* / \int_0^1 du^*$) yields the following for the vorticity centroid, \bar{r}^* :

$$\bar{r}^* = \frac{1}{n} \int_0^1 r^* (1 - r^*)^{(1/n)-1} dr^*, \quad (8)$$

where the integral term can be evaluated in terms of the beta function. Simplification gives the centroid

$$\bar{r}^* = \frac{n}{n+1}. \quad (9)$$

Hinze²⁷ indicates that $n=7$ is applicable for a wide range of Reynolds number for the fully developed turbulent flow; $n=7$ is used for our studies; thus, $\bar{r}^* = 0.875$.

B. Vortex ring strength

For all simulations, the strength of the imposed vorticity, which imposes vortical velocities shown in Eq. (5), is based on circulation across the boundary layer for fully developed turbulent pipe flow. The most dominant wavelength caused by boundary-layer instability is used for approximating the circulation of the vortex ring at the nozzle exit.¹⁸ Thus,

$$\Gamma_v = U\lambda. \quad (10)$$

The boundary layer wave is approximated using the Brennen²⁸ theory, $\lambda = (2\pi/\gamma)\delta_2$, where $\gamma = 0.175$, and δ_2 is the momentum thickness of the turbulent flow. The momentum thickness, δ_2 ,²⁹ is evaluated analytically using the power-law velocity profile of Eq. (7). Thus,

$$\delta_2 = \int_{r=0}^{r=a} \left(1 - \frac{u}{U}\right) \frac{r}{a} \frac{u}{U} dr = \frac{3n^2}{2(2 + 7n + 7n^2 + 2n^3)} a, \quad (11)$$

where $n=7$, and, thus, $\delta_2/a \approx 0.07$. This value is in agreement with Salami's³⁰ experimental and analytical studies. Salami also found the asymptotic behavior of the momentum thickness at $\delta_2/a \approx 0.07$ for the fully developed, turbulent-pipe flow.

C. Pulsation due to turbulence

Fluctuations in the initial velocity field play a significant role in initiating instabilities once fluid leaves the nozzle. To provide an impetus for these instabilities, the mean jet velocity is pulsed sinusoidally with a small amplitude, A , according to

$$U = U_0[1 + A \sin(\omega t)], \quad (12)$$

where U_0 is the nominal center-line velocity, and ω is the angular frequency. The selected angular frequency corresponds to the dominant wavelength for boundary-layer instabilities, $\lambda = (2\pi/\gamma)\delta_2 = 2.45a$ or $\omega a/U_0 = 0.816\pi$.²⁸ This frequency was selected because velocity fluctuations are expected to be predominantly initiated by boundary-layer instability within the pipe.³¹ In these relations, δ_2 is the boundary-layer momentum thickness. The dominant wavelength corresponding to boundary-layer instability differs by noninteger factors from that of the Kelvin-Helmholtz instabilities that drive subsequent fluctuation growth. Smaller scale fluctuations at these frequencies are not expected to strongly affect the flow evolution. In Sec. VII, we will show that the droplet distribution results are insensitive to the amplitude and frequency of the initial velocity fluctuations for amplitudes that are an order of magnitude greater and more. The results presented in Sec. VI employ $A=0.01$.

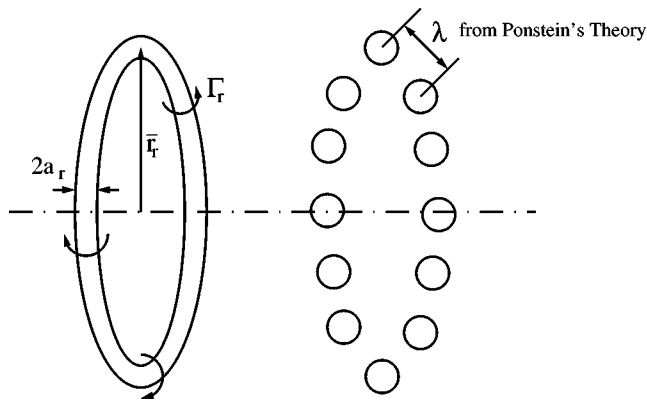


FIG. 3. Secondary instability model using Ponstein's linear theory (Ref. 6).

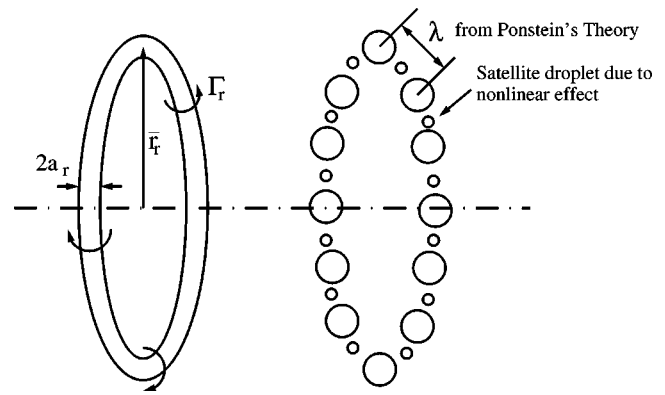


FIG. 4. Secondary instability model due to nonlinear effect.

IV. MODELING THE SECONDARY INSTABILITY

While the BEM portion of the model is based on an axisymmetric formulation, atomization is a three-dimensional (3D) phenomenon. The BEM portion of the model results in pinch-off is not of a droplet, but of a vortex ring with circulation around the ring surface, which is sufficient to cause instability in the circumferential direction. In reality, this is a 3D secondary instability that occurs before the vortex-ring pinch-off. The current model assumes droplets are formed from a secondary instability on annular ligaments shed from the jet periphery, as shown in Fig. 3. This modeling amounts to decoupling primary (2D) and secondary instability (3D), which permits an axisymmetric analysis of the jet itself. This type of ring analysis, which decouples the dimensionality between an axisymmetric ring and 3D “fingerlike” droplets, often is used to predict the number of droplets (or “fingers”) generated in the azimuthal direction.^{18,32–34} Mehdizadeh *et al.*³⁴ confirms, analytically and experimentally, validation of the applicability of the Rayleigh–Taylor instability theory (based on linear analysis) for predicting the number of “fingers” around the ring edge. Mehdizadeh *et al.*³⁴ found the fastest growing wave in the circumferential direction as a function of Weber number. Kim *et al.*³² assumed an immediate production of droplets from the ring, whose assumption was justified based on the experimental observations of Range and Feuillebois.³⁵ We, too, apply a similar methodology of Kim *et al.*³² and Mehdizadeh *et al.*³⁴ using the Ponstein's linear theory⁶ to predict the fastest growing wave in the circumferential direction around the ring edge for the liquid jet.

Ponstein's⁶ linear analysis is used to describe instability of the vortex ring. The most unstable wave number, k , is found implicitly from the maximum growth rate, ω . In dimensionless form, the relationship between k and ω is

$$\omega^{*2} = \left[\frac{1 - k^{*2}}{\text{We}_r} + \left(\frac{\Gamma_r^*}{2\pi} \right)^2 \right] k^* \frac{I_1(k^*)}{I_2(k^*)}, \quad (13)$$

where $\omega^* = \omega a_r / U$, $k^* = k a_r$, $\Gamma_r^* = \Gamma_r / (U a_r)$, a_r is the pinched-off ring radius. $I_1(k^*)$ and $I_0(k^*)$ are modified Bessel functions of the first kind. We_r is the ring Weber number defined as

$$\text{We}_r = \rho u_i^2 a_r / \sigma, \quad u_i = U + u', \quad (14)$$

where u' is an instantaneous value of the fluctuating component of velocity modeled as a simple harmonic function,³⁶

$$u' = A U \sin(2\pi R N), \quad (15)$$

where A is an amplitude coefficient, and $A = 0.01, 0.10, 0.20$, and 0.40 for this study. Here the pulsation magnitude, A , is the same parameter as in Eq. (12) because it is assumed that the turbulence intensity at the nozzle exit is proportionally propagated to the vortex ring to induce instability. $R N$ represents the random number designed to introduce randomness in the droplet size distribution. The solution of Eq. (13) yields the most unstable wave number ($k a_r$), determining the number of droplets (N) resulting from the breakup of this specific ring. The droplet diameter for all droplets, resulting from the breakup of each ring, is distributed equally among that many droplets.

It is noteworthy that a nonlinear instability analysis will lead to multiple crests per wavelength^{37,38} and subsequent smaller satellite drops as indicated in Fig. 4. In the present work, we ignore the nonlinear effect of this sort. As a consequence, we expect to underestimate the number of smaller droplets. We will address this issue beginning in Sec. VI.

V. EXPERIMENTS

For model evaluation, a water spray was produced using a converging nozzle manufactured by Spraying Systems Co., Wheaton, IL.² The internal converging angle was approximately 40 degrees, and followed by a constant-diameter section 3.31 mm in length. Multiple vanes were installed inside the nozzle, enhancing turbulence mixing. This water spray was directed horizontally, with a liquid core velocity of $U_{inj} = 80$ m/s, a diameter of $d = 2$ mm, a mass flow rate of $\dot{m} = 0.25$ kg/s, and a liquid and surrounding air temperature of $T = 300$ K. A photograph of this high-pressure water spray is shown in Fig. 5.

For a high velocity jet, turbulent spray measurements of droplet velocity and size were extremely difficult to obtain near the liquid core. The length of the liquid core was relatively short for these turbulent sprays, leading to a dense, initial droplet field that obscured optical access to the spray's interior. This feature made the present phase Doppler particle

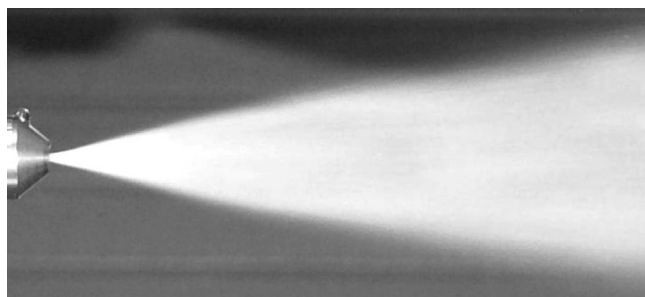


FIG. 5. Experimental image of near field view of water jet in the atomization regime (Ref. 2).

analyzer (PDPA) measurements virtually impossible in the near field. For this reason, experimental data were collected downstream of the spray nozzle at $x=48\text{ mm}=24d$. Experimental data include average droplet size (D_{10}), Sauter mean diameter (D_{32}), and average droplet velocity (U_D). There are uncertainties associated with each of these measurements. Generally, the two variables (D_{10} and U_D) contain an error of approximately 10%–15% according to our current PDPA experience.

The experimental data are summarized in Table I. It shows data collected at five different radial locations (i.e., $y=0, 5, 10, 15,$ and 20 mm) for $x/d=24$. Several observations can be made from these experimental data. First, the average droplet diameter (D_{10}) tends to be larger at larger radii for each downstream location. The droplets are well segregated radially at this downstream axial location, $x/d=24$. Thus, the size distribution width is narrower (i.e., larger dispersion coefficient, q) as the radial location increases. This type of droplet gradation is due to different dynamic behavior of small and large droplets and, to entrainment of airflow. Second, the droplet velocity decreases at larger radii as drag reduces it. While analysis for the experimental data is concisely discussed in Ref. 2, the data are further explored and investigated in Sec. VI.

In Table II, the experimental data collected at various axial locations are summarized. Under the cone angle, approximately $\theta\cong 15^\circ$, the width of the jet increases as the axial location increases. Both D_{10} and D_{32} also grow with increasing the axial location because of the gradual disappearance of the smaller droplets further downstream. Smaller droplets have a tendency to quickly evaporate, and coalescence also causes a shift to larger droplet sizes downstream. The rate at which D_{32} growth from $x=48\text{ mm}$ to x

TABLE I. Experimental data collected at downstream of the nozzle at $x=48\text{ mm}=24d$ for various radial (y) locations.^a

Radial location (mm)	$y=0$	$y=5$	$y=10$	$y=15$	$y=20$
D_{10} (μm)	32.29	43.33	43.08	43.86	54.76
D_{32} (μm)	68.92	71.19	69.71	64.95	71.19
q	1.288	1.747	1.784	2.043	2.651
\bar{U}_D (μm)	69.91	64.84	50.97	35.79	32.36

^aNote, nozzle diameter, $d=2\text{ mm}$, jet velocity, $U_{\text{jet}}=80\text{ m/s}$, and Weber number, $We=87\,193$. Here, q was the dispersion coefficient defined in Sec. IV. D_{32} represented Sauter mean diameter.

TABLE II. Experimental data collected at various axial locations.^a

x (mm)	0	48	250	480	810
Δy (mm)	1	20	90	125	170
D_{10} (μm)	40.63	46.85	72.39	79.66	71.60
D_{32} (μm)	75.78	83.49	90.77	117.71	119.41
D_{32}/D_{10}	1.865	1.782	1.254	1.478	1.668
q	1.496	1.576	2.910	2.050	1.712

^aNozzle diameter is $d=2\text{ mm}$. At nozzle exit ($x=0\text{ mm}$), both D_{10} and D_{32} are extrapolated.

$=480\text{ mm}$ is greater than that of D_{10} . This pattern indicates the existence of relatively larger droplets dominating at a downstream location as D_{32} is greatly affected by the larger droplets (i.e., $D_{32}\propto D^3/D^2$). Evaporation plays a role in reducing D_{10} at $x=810\text{ mm}$ as surrounding air causes droplets to quickly evaporate further downstream. Using the downstream data of Table II, the droplet data at the nozzle exit (i.e., $x=0$) are extrapolated. As this type of extrapolation technique was previously shown to have merits in providing initial conditions,² the extrapolated arithmetic mean droplet size, $D_{10}=40.63\text{ }\mu\text{m}$ is used for spray simulations using the SSF model. In addition, these extrapolated data will be compared with the prediction from the BEM liquid core model in Sec. VI.

VI. LIQUID BREAKUP SIMULATIONS

Simulations of the liquid core breakup process, leading to an initial distribution of droplet sizes and velocities, are presented in this section, which focuses on the effect of the Weber number on the droplet distributions. Subsequent sections will address the sensitivity of droplet distributions to perturbations of the initial liquid core flow.

A. Droplet size and velocity distributions

The Weber number represents competition between the dynamic force and surface tension force. It is well known that the surface tension force plays an important role in stabilizing the low speed jet in the Rayleigh flow regime.¹¹ At relatively high speeds, dynamic forces become significant, leading to instabilities and, therefore, the liquid jet breakup occurs. The Weber number determines the balance between these behaviors with larger initial Weber numbers generally leading to smaller droplets in the end. This result is primarily a function of the Weber number dependence on the jet velocity. For a greater jet velocity, the critical Weber number below which breakup is unlikely occurs for a smaller droplet diameter. In this manner, the droplet size and its distribution (PDF) vary significantly depending on the jet velocity. Unfortunately, there are no reports on the PDF variation of the droplet size and velocity at the liquid core region. In this section, computed PDFs in the liquid core region are presented and compared with various presumed shape PDFs.

Simulations are conducted using the methods described in Secs. II–IV with the initial jet Weber number, Eq. (3), taking on values of 10 000, 25 000, 50 000, and 87 193. The latter Weber number, $We=87\,193$, corresponds to the experi-

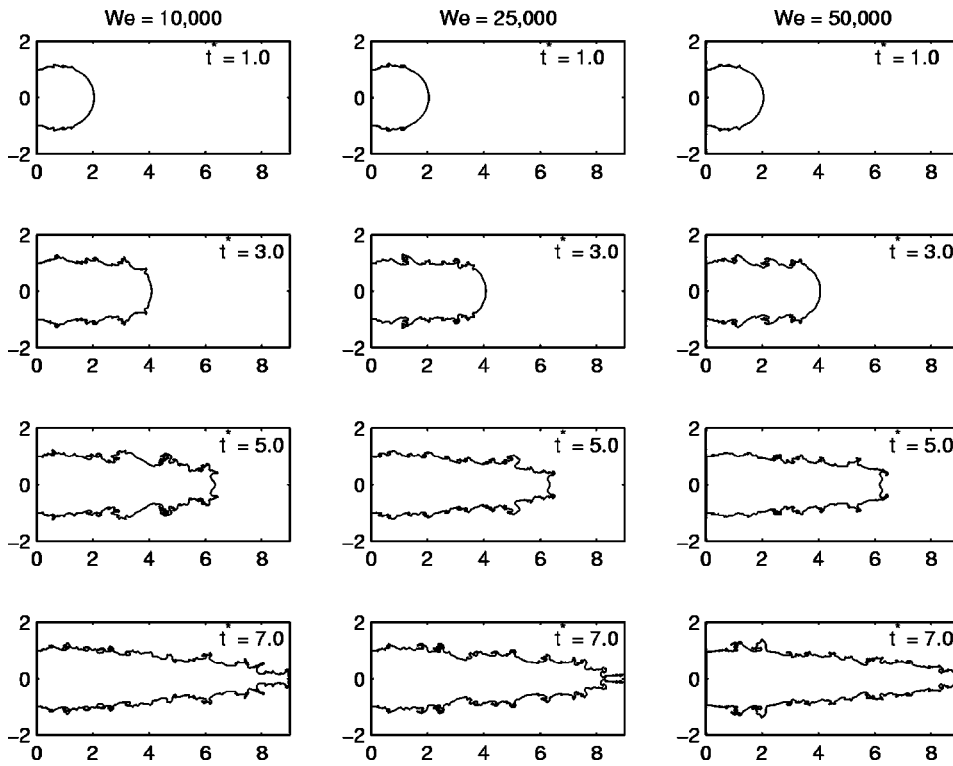


FIG. 6. Simulations of evolution of the jet at various Weber numbers. Here t^* is a dimensionless time, defined as $t^* = tU/a$. In a given period of physical time, the mass loss of the higher velocity jet (i.e., $We = 10\,000 < 25\,000 < 50\,000$) is much greater. The physical time corresponded to $t^* = 7$; $t = 0.259, 0.164, \text{ and } 0.116$ ms for $We = 10\,000, 25\,000, \text{ and } 50\,000$, respectively.

mental measurements described in Sec. V. The liquid core evolution is shown in Fig. 6 for the first three cases. Here, $t^* = 7$, is a dimensionless time, defined as $t^* = tU/a$, which corresponds to the physical time, $t = 0.259, 0.164, \text{ and } 0.116$ ms for the Weber number of $We = 10\,000, 25\,000, \text{ and } 50\,000$, respectively. In terms of physical time, the case with higher Weber number loses much more mass and, thus, more droplets are launched. Naturally, a “thinner” liquid core is shown as the higher mass flow rate with the given fluid and fixed nozzle diameter. It is important to remember the jets are pulsed with a pulsing magnitude of $A = 0.01$. Clearly, the pulsing frequency has no significant effect on the jet surface shape in the high-velocity regime under the given pulsing magnitude, $A = 0.01$; no visible pulsed waves appear on the free surface. Key results from these simulations are summarized in Table III; statistics in Table III are collected over $\Delta t = 0.26$ ms duration. The simulations capture the expected reduction in the mean diameter with increasing Weber number or jet velocity.

Among many presumed-shape PDFs in the literature,⁴ we have chosen the three most popular distributions: the Rosin–Rammler, log-normal, and Nukiyama–Tanasawa (NT) models. These distributions are mathematically simple (thus practical to use) and have yielded reasonable results in the past. The Rosin–Rammler distribution is defined as

$$f(D) = \frac{qX^{q-1}}{X^q} \exp\left[-\left(\frac{D}{X}\right)^q\right], \quad (16)$$

where X and q are parameters determining the distribution shape. The distribution can be shifted to larger or smaller droplet sizes by varying X , which is related to the arithmetic mean diameter, D_{10} , as follows:

$$X = \frac{D_{10}}{\Gamma\left(\frac{1}{q} + 1\right)}. \quad (17)$$

The log-normal distribution is defined as

$$f(D) = \frac{1}{\sqrt{2\pi}\sigma_{\ln}^* D} \exp\left[-\frac{[\ln(D/D_{\ln})]^2}{2\sigma_{\ln}^{*2}}\right], \quad (18)$$

where σ_{\ln}^* is the nondimensional standard deviation of the logarithm of the diameter. $D_{\ln} = \exp[\ln D]$ is the log-normal

TABLE III. Computational results under different Weber numbers.^a

Cases	1	2	3	Yoon <i>et al.</i> (Ref. 2)
We	10 000	25 000	50 000	87 193
A	0.01	0.01	0.01	0.01
U (m/s)	27.02	42.72	60.42	80.00
\bar{U}_D (m/s)	23.32	37.04	51.71	71.90
$\Delta U_{\text{jet} \rightarrow D}$ (%)	13.69	13.30	14.41	10.13
$U_{D,\text{rms}}$ (m/s)	7.19	10.53	14.74	21.27
D_{10} (μm)	50.89	46.06	41.48	39.97
$D_{10,\text{rms}}$ (μm)	28.49	27.32	24.97	24.46
D_{32} (μm)	89.06	85.97	78.90	76.82
q	1.611	1.495	1.464	1.412
N_{drop}	66 222	153 926	276 348	493 390
\dot{m}_{drop} (kg/s)	0.0176	0.0303	0.0397	0.0635
\dot{m} (kg/s)	0.0845	0.1342	0.1898	0.2513
$f(\dot{m}) = \dot{m} / \dot{m}_{\text{drop}}$	4.83	4.43	4.78	3.96

^aNote that nozzle diameter was $d = 2$ mm. Cross-sectional area, $A_1 = \pi \times 10^{-6}$ m². Statistical details were collected during the physical time, $\Delta t = 0.26$ ms. Liquid was water, thus, $\rho = 1000$ kg/m³.

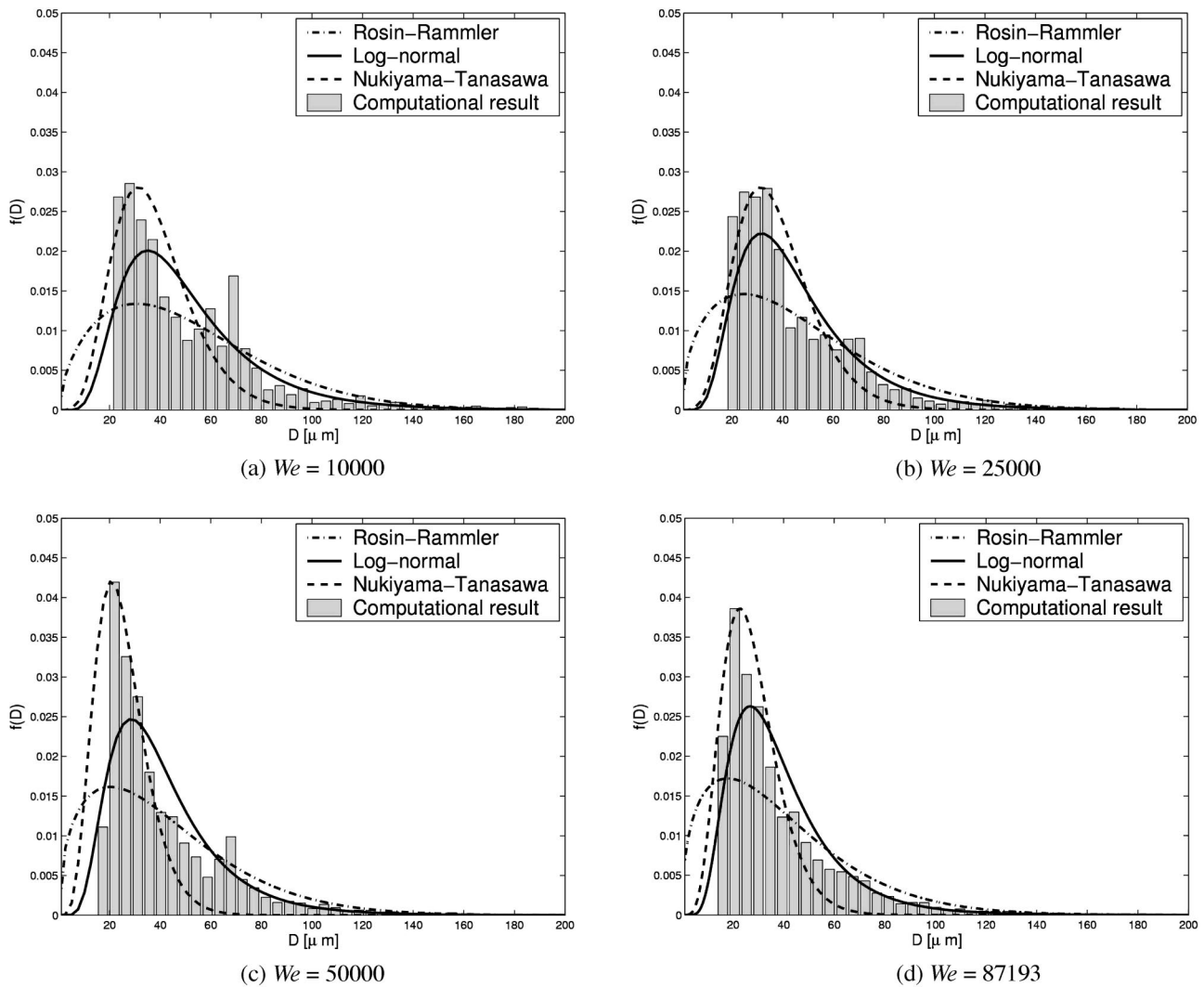


FIG. 7. Simulations of droplet-size distribution at various Weber numbers. (a) $We=10\,000$, (b) $We=25\,000$, (c) $We=50\,000$, (d) $We=87\,193$.

diameter defined as the exponent of the logarithm average. Kuo and Corsin³⁹ provide the relation between D_{ln} and D_{10} ,

$$D_{ln} = \frac{D_{10}}{\exp\left[\frac{\sigma_{ln}^{*2}}{2}\right]}. \quad (19)$$

The NT distribution is defined as

$$f(D) = aD^p \exp[-bD^c], \quad (20)$$

where b , p , and c are adjustable parameters, and a is a normalizing factor defined as $a = b^{(p+1)/c} / \Gamma[(p+1)/c]$. Here, c is arbitrarily taken to be fixed at $c=1$, while the permissible range of p and b are $2 \leq p \leq 5$ and $0.08 \leq b \leq 0.22$, respectively.

In Fig. 7, the three presumed-shape PDFs for various Weber numbers are compared with the droplet size PDF from the liquid core model. For the presumed-shape PDFs, the computed average droplet size, D_{10} , from the liquid core model is used for all presumed-shape PDFs input. For the Rosin-Rammler distribution, the dispersion coefficient, q , is obtained from the computed values of D_{10} and D_{32} (Table

III) using moments of the Rosin-Rammler droplet size distribution [i.e., $\int_0^\infty D^n f(D) dD = X^n \Gamma(n/q+1)$ in Ref. 40],

$$f(q) = \frac{D_{32}}{D_{10}} = \frac{\Gamma\left(\frac{3}{q} + 1\right)}{\Gamma\left(\frac{1}{q} + 1\right)\Gamma\left(\frac{2}{q} + 1\right)}. \quad (21)$$

Similar methodology is applied for the log-normal and the NT distributions to estimate relevant coefficients corresponding to the computed PDFs of the BEM liquid core model.

The presumed-shape PDFs are compared with the computed PDFs in Fig. 7. The agreement is found to vary depending on the particular fitting criteria selected. When the distribution peak is matched (as with the NT distribution), the agreement with the majority of the droplets is observed to be good, but the agreement is less suitable for the distribution tails. When the computed values of D_{10} and D_{32} are used, the agreement of the tails of the PDF is greatly improved. A better agreement is found as jet velocity increases, the probability of smaller droplets became higher because the smaller length scale starts to dominate within the flow.

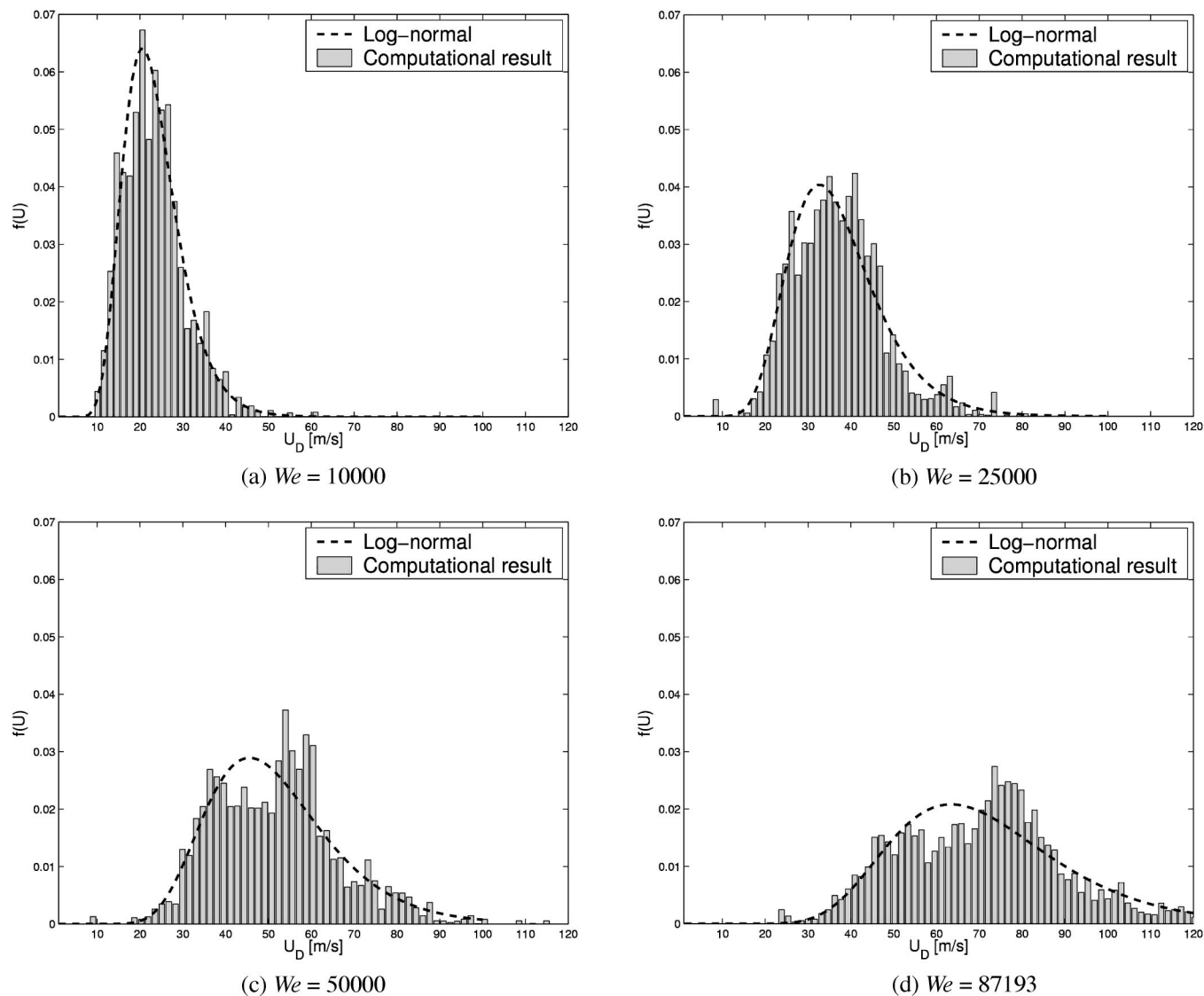


FIG. 8. Simulations of droplet-velocity distribution at various Weber numbers. (a) $We=10\,000$, (b) $We=25\,000$, (c) $We=50\,000$, (d) $We=87\,193$.

For the wide range of Weber numbers (i.e., $10\,000 < We < 87\,193$), droplet size distributions are in reasonable agreement with the NT model, except the NT model neglects some large droplets distribution in the lower-right region of the computational results obtained using the BEM liquid core model (whose issue we will address in detail in Sec. VI C). Other than that, their comparisons seem to be in good agreement. The log-normal model seems to be a reasonable approximation as well, except for the highest “peak” located in the left (or smaller size) side of the distributions. Overall, it is reasonable to state that the NT and the log-normal distributions can best describe droplet size distribution at the liquid core for the wide range of Weber numbers.

Distributions for droplet velocity are shown in Fig. 8 for the various Weber numbers. As jet velocity increases, the distribution width becomes larger. It is because the length scale associated with the primary atomization for the higher jet velocity is multitudinous, while that of the lower jet velocity is mainly driven by one dominant length scale (i.e., boundary layer instability). In addition, the larger velocity

fluctuation of droplets is due to the larger turbulence fluctuation at higher jet velocity (see $U_{D,rms}$ in Table III). Overall, it is fair to state that the log-normal model can satisfactorily describe the velocity distribution for the wide range of Weber numbers. Therefore, the log-normal distribution is recommended as an initial droplet velocity at the liquid core region.

In Fig. 9, the computational prediction for the arithmetic mean droplet size, D_{10} , from the BEM liquid core model is compared with extrapolated experimental data. As shown, the prediction of the BEM liquid core model for D_{10} is within 2% error for the case $We=87\,193$. No scaling constant was used for our liquid core model. This excellent comparison is a strong evidence that boundary-layer instability alone characterizes the droplet size distribution completely for the water-into-air type spray. It is reminded that the BEM liquid core model considers the boundary layer instability only; no shear-layer driven [i.e., Kelvin–Helmholtz (KH) type] instability between the liquid and gas are taken into account for the model. Contrary to traditional thought (that is

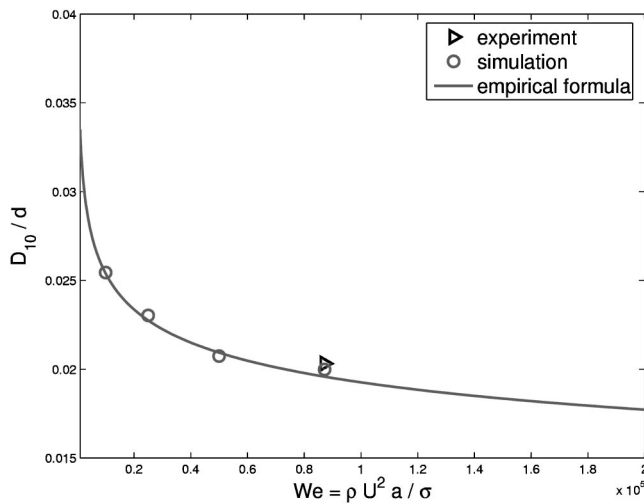


FIG. 9. The initial average droplet size (D_{10}) at the liquid core; experiment, simulation, and the empirical formula.

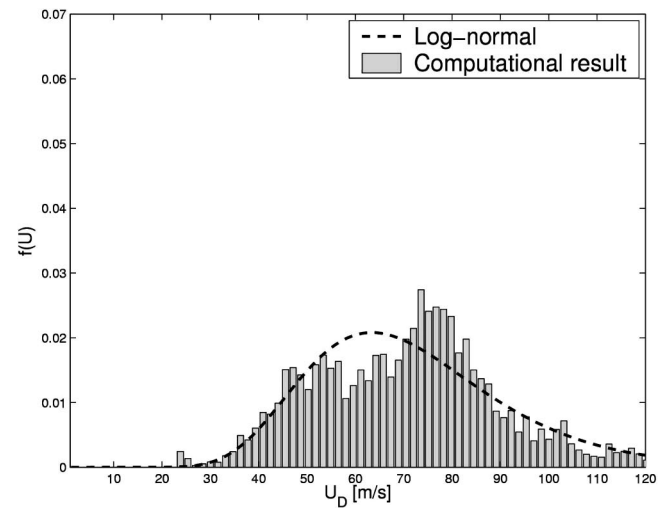
KH type instability is greatly responsible in characterizing droplet distribution), the intuitive thinking suggests there is not enough room for an air to occupy in the liquid core region, where the continuous slug of fluid becomes atomized and generates countless numbers of droplets in the region. This liquid core region is so dense that it almost acts as a continuous fluid. Consequently, neither can air be trapped substantially in the region, nor can it play some significant role in causing the primary atomization.

Moreover, small amount of trapped air in the liquid core region is moving at the launched droplet velocity due to entrainment; thus, there is no relative velocity, U_{rel} , between the droplets and the air. In such case (i.e., $U_{rel} \approx 0$), KH instability suggests that the growth rate is imaginary and, therefore, the jet is unconditionally stable. Ironically, the KH instability suggests that KH instability mechanism is not responsible for the atomization mechanism in the liquid core region. Thus, some other instability mechanism must be playing an important role, which we believe it is the boundary layer instability. Comprehensive reports on the boundary layer instability as well as the shear-layer driven instability are reviewed in Ref. 41. The empirical formula is constructed in Eq. (22) using the similar technique of Wu *et al.*⁴² except we have adopted the boundary layer length scale of Brennen,²⁸

$$D_{10} = \frac{C\lambda}{We^{0.12}} \left(\frac{a}{\lambda} \right)^{0.12}, \quad (22)$$

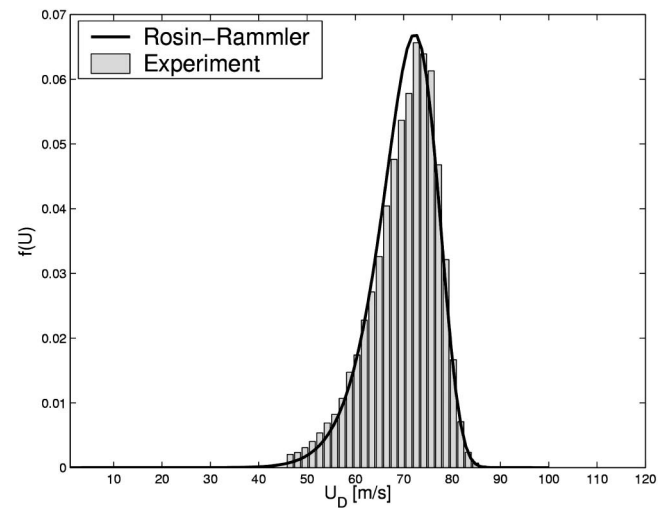
where the boundary layer wavelength, $\lambda = (2\pi/\gamma)\delta_2$ (λ is in the unit of meter) can be estimated using the Brennen's²⁸ most unstable dimensionless frequency of the boundary layer separating flow, $\gamma = 0.175$. The adjustable constant is $C = 0.068$ and a represents the nozzle radius. Note that D_{10} is in the unit of meter. This empirical formula can be used to estimate the initial average droplet size at the nozzle exit for the turbulent spray of our nozzle type.

Summarizing statistical details from simulation results obtained for various Weber numbers, Table III indicates that the standard deviation of the droplet velocity rose with in-



(a) Computational result at liquid core

$\bar{U}_D = 69.27 \text{ m/s}$, $\sigma_{in}^* = 0.5$ is used



(b) Experimental result at $x = 48 \text{ mm}$ at the centerline ($y = 0 \text{ mm}$).

$\bar{U}_D = 69.91 \text{ m/s}$, $q = 13.2$ is used.

FIG. 10. Comparison of the droplet velocity distribution at the center line for the $We = 87193$ case. (a) Computational result at liquid core; $\bar{U}_D = 69.27 \text{ m/s}$. The dimensionless log-normal standard deviation $\sigma_{in}^* = 0.5$ is used. (b) Experimental result at $x = 48 \text{ mm}$ at the center line ($y = 0 \text{ mm}$); $\bar{U}_D = 69.91 \text{ m/s}$. The dispersion coefficient $q = 13.2$ is used.

creasing the jet velocity. It is noteworthy that the droplet velocity is about 10%–15% less than the jet velocity, which seems consistent with the observation of Wu *et al.*⁴² for their turbulent jet. Wu *et al.*⁴² found that the droplet velocity was generally 15%–25% less than the jet velocity near the nozzle exit for a wide range of jet velocity. In the case of Wu *et al.*,⁴² the droplets experienced drag while the droplet velocity of our computation is recorded as soon as the droplets are separated from the liquid core. Thus, it is natural that Wu's droplet velocity was slightly smaller than that of our computational result. A possible reason for the droplet velocity being less than the jet speed is that the vorticity interaction near the liquid jet surface retards the motion of turbulent eddies.⁴² The local circulation, proportionally scales with the local droplet velocity, generally is not large enough to induce

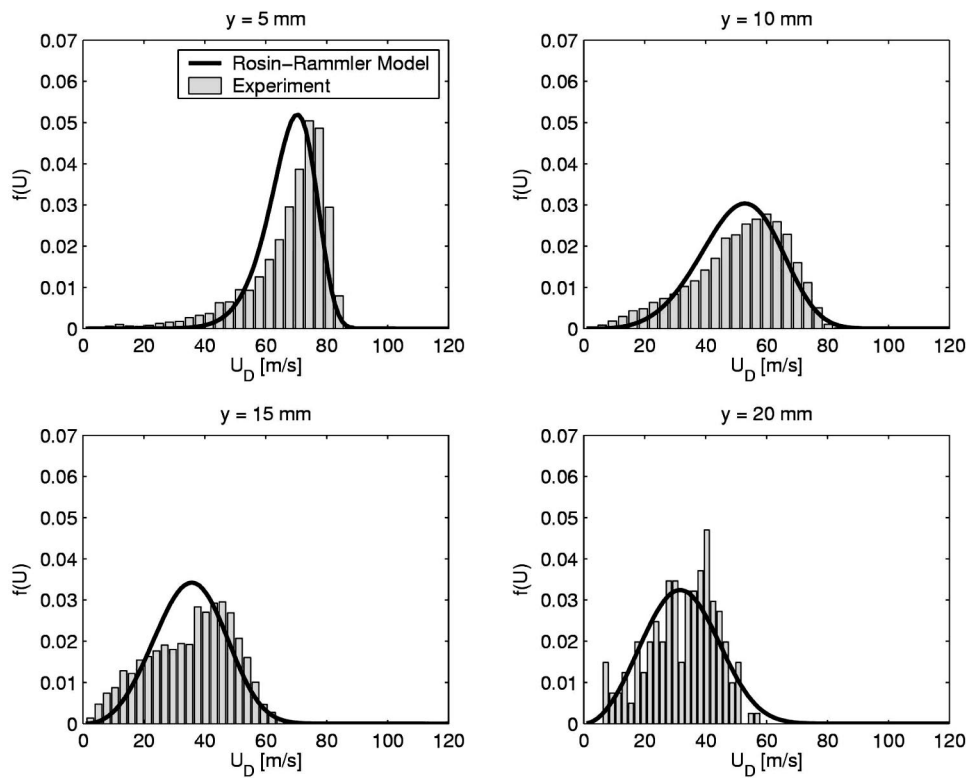


FIG. 11. Experiment of the droplet velocity distribution at various radial locations (i.e., $y=5, 10, 15,$ and 20 mm) at the axial location of $x=48$ mm for the $We=87\,193$ case. The Rosin-Rammler model is used to compare the experimental data. The corresponding dispersion coefficients are $q=10.0, 4.5, 3.5,$ and 3.0 for $y=5, 10, 15,$ and 20 mm, respectively.

an added velocity on the droplets separated from the liquid core unless the local circulation is enhanced by some external forcing source. In Sec. VII, we will show that the overall droplet velocity can be larger than the jet velocity when a periodic injection is enforced on the jet with sufficiently larger fluctuation magnitude.

It is noteworthy that the variation of the Sauter mean diameter (D_{32}) is not as significant as the arithmetic average diameter, D_{10} , as shown in Table III. It is perhaps due to the gradual disappearance of larger droplets with increasing the jet velocity (see Fig. 7). In addition, the standard deviation for the droplet size is decreasing at higher jet velocity, which indicates that a certain small-length scale starts to dominate. This kind of asymptotic behavior of the droplet characteristics with increasing jet velocity has widely been observed by various authors.^{18,42}

Table III shows that the droplet size became slightly more dispersive (i.e., smaller q) when the jet velocity increased. The $f(q)$ and q were inversely proportional; the increase in $f(q)$ resulted in a decrease of q . Thus, the larger ratio of D_{32} and D_{10} indicates that the effect of larger droplets (which led to more dispersive behavior of droplet statistics) became more prominent for the higher-velocity case. Table III also shows that about one-half million droplets are produced within about one-quarter millisecond for the $We=87\,193$ case. While the relationship between the Weber number and the droplet number, N_{drop} , is nearly linear, the relationship between the jet velocity (U) and N_{drop} is quadratic (i.e., $We \propto U^2$). The mass flow rate, \dot{m}_{drop} is estimated using the collected droplet number and its value compared with the total mass flow rate, \dot{m} . Their ratio, $f(\dot{m})$, which can be regarded as dimensionless mass flow rate, indicates that from 20%–25% of the total mass is lost due to droplet

launching at the time when the statistics are collected. Here, the collected mass flow rate is defined as $\dot{m}_{\text{drop}} = \rho(\pi D_{\text{avg}}^3/6)N_{\text{drop}}/\Delta t$, while the mass flow rate is $\dot{m} = \rho U A_x$.

B. Droplet gradation

Yoon *et al.*² showed that droplet gradation occurs due to the dynamic segregation of small and larger droplets in both the axial and radial directions. Larger droplets are dispersed by the spray initial cone angle and subsequent interactions with turbulent eddies in the entrained air, while smaller droplets are generally swept toward the spray center line by aerodynamic drag interactions with the entrained air. In addition, coalescence and evaporation phenomenon enhances the droplet segregation process by favoring the presence of the larger droplets. Coalescence event in upstream location increases the presence of larger droplets downstream. The evaporation rate for small droplets is quicker than for larger ones because the droplet evaporation is known to obey the classical D^2 law.⁴³ As a result, the overall droplet size increases downstream. Thus, it is clear that all of these multiphysics of flow contribute to the droplet gradation phenomenon. While the results of Yoon *et al.*² support the droplet gradation phenomenon (which occurs in the entire spray region), our investigation focuses on droplet gradation, especially near the liquid core region. As mentioned earlier, optical access to the liquid core region using the current PDPA technique is impossible, and, thus, the axial location $x/d=24$ at the center line ($y=0$ mm) was the closest to the nozzle that we could approach. When the experimental data obtained at the axial location $x=48$ mm= $24d$ are compared to computational results obtained at the liquid core (approx-

mately, $x < 8$ or 10 mm), we confirm the droplet gradation phenomenon, which occurs as soon as droplets are separated from the liquid core.

Computational result for droplet velocity distributions at the liquid core is shown in Fig. 10(a). The experimental data obtained at $x/d=24$ downstream at the center line ($y=0$ mm) are shown in Fig. 10(b). This is another reminder that the results in Figs. 10(a) and 10(b) are not obtained at the same axial location since it is impossible to obtain the experimental PDF of the droplets at the liquid core with current imaging technologies.²⁴ The objective of the comparison is to show the droplet gradation phenomenon, which occurs from the liquid core to the downstream location, $x/d=24$. As shown in Fig. 10, the distribution width of computational results at the liquid core is relatively larger than the experimental data obtained downstream, $x/d=24$. At the liquid core surface, droplets of various sizes are launched. Larger droplets generally carry greater momentum. These launched droplets of various sizes start to gradate rapidly due to different dynamic behavior. Large droplets are dispersed outwardly, while smaller droplets generally are swept toward the spray center line by aerodynamic drag interactions with the entrained air. However, these entrained smaller droplets maintain their launching velocity in the axial direction because (1) these small droplets are surrounded by the larger droplets and, thus, preserve their initial velocity, and (2) the entrained air affects the radial velocity of the small droplets only, not the axial component of the velocity. As for the droplet velocity distribution, Fig. 10 shows that the distribution evolves from the log-normal shape at the liquid core to the Rosin–Rammler shape at downstream, $x/d=24$ because of the droplet gradation. In Fig. 11, additional experimental data for droplet velocity distribution at various radial locations (i.e., $y=5, 10, 15$, and 20 mm) are shown. As the radial location increases, the droplet velocity is reduced because of drag. While the droplets, surrounded by moving neighboring droplets, preserve the initial launching velocity, those located at the outer radial locations are susceptible to more drag. It was interesting to observe the experimental results for all radial locations are in good agreement with the Rosin–Rammler model.

In Fig. 12, the droplet size distribution at the liquid core [Fig. 12(a)] and that obtained at $x/d=24$ [Fig. 12(b)] are compared. While both distributions are in fairly good agreement with the NT distribution model, the arithmetic mean droplet (D_{10}) size of the liquid core is larger than that obtained downstream, $x/d=24$ (compares centerline results in Table I and the $We=87\,193$ case in Table III). This pattern confirms that the smaller droplets conglomerate toward to the center line by the time the droplets reach $x/d=24$. Such gradation phenomenon is experimentally manifested in Table I; the mean droplet size increases by as much as 36% when the radial location increases from $y=0$ to 20 mm. In Fig. 13, size distributions for various radial locations are shown. It is interesting to observe that both size and velocity distributions of experimental data are in fairly good agreement with the Rosin–Rammler distribution model at the downstream region, $x/d=24$.

In an effort to reveal the relationship between the droplet

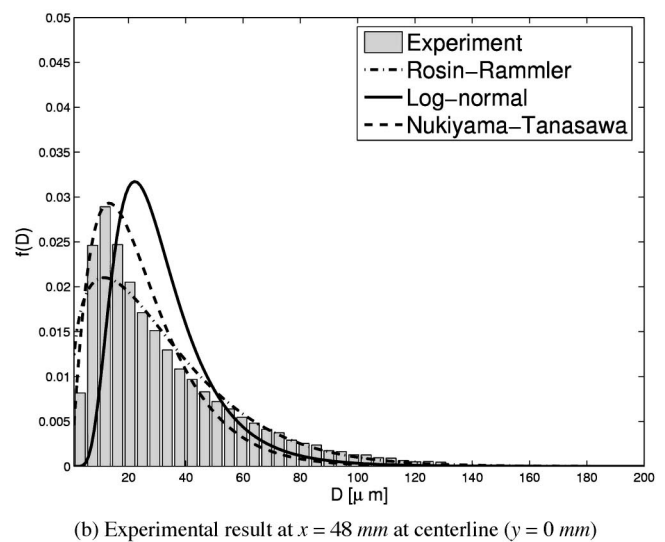
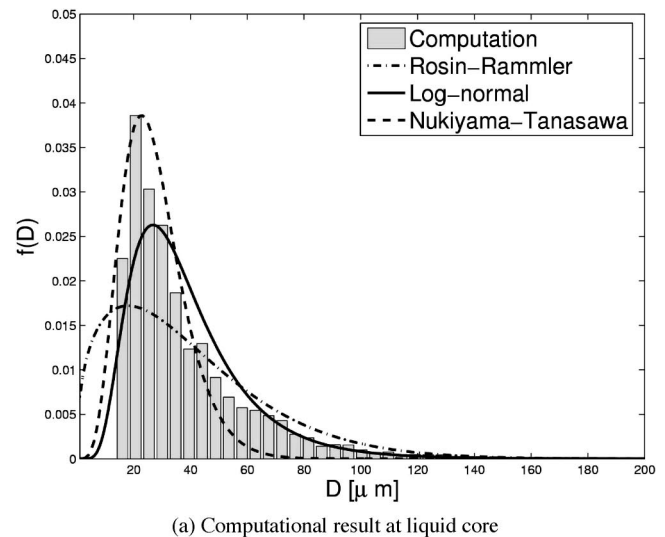


FIG. 12. Comparison of the droplet-size distribution at the center line for the $We=87\,193$ case. (a) Computational result at liquid core. (b) Experimental result at $x=48$ mm at center line ($y=0$ mm).

size and velocity, joint PDFs (JPDF) of droplet size and velocity are plotted for the liquid core in Fig. 14(a) and for the $x/d=24$ downstream in Fig. 14(b). The noisy behavior of the JPDF at the liquid core indicates that the liquid core in nature is random and chaotic. The range of the droplet velocity of relatively high PDF is around $65\text{ m/s} \leq U_D \leq 85\text{ m/s}$. It also is shown in Fig. 14(a) that some small droplets have fairly high velocity (i.e., $U_D > 100\text{ m/s}$) even though the individual droplet momentum is proportional to the droplet size, as shown in Fig. 15. Droplets in the range of $20\text{ }\mu\text{m} \leq D \leq 30\text{ }\mu\text{m}$ have relatively high PDF values. In Fig. 14(a), the droplet velocity is reduced when increasing the droplet size for the smaller droplets; momentum loss occurs. On the other hand, the droplet velocity is increased when increasing the droplet size for the larger droplets; momentum gain occurs. In the end, these droplets tend to equalize their velocity at about $65\text{ m/s} \leq U_D \leq 85\text{ m/s}$. This “equalizing” behavior is manifested in Fig. 14(b) of the data collected at downstream, $x/d=24$. By the time the droplets reach $x/d=24$ downstream

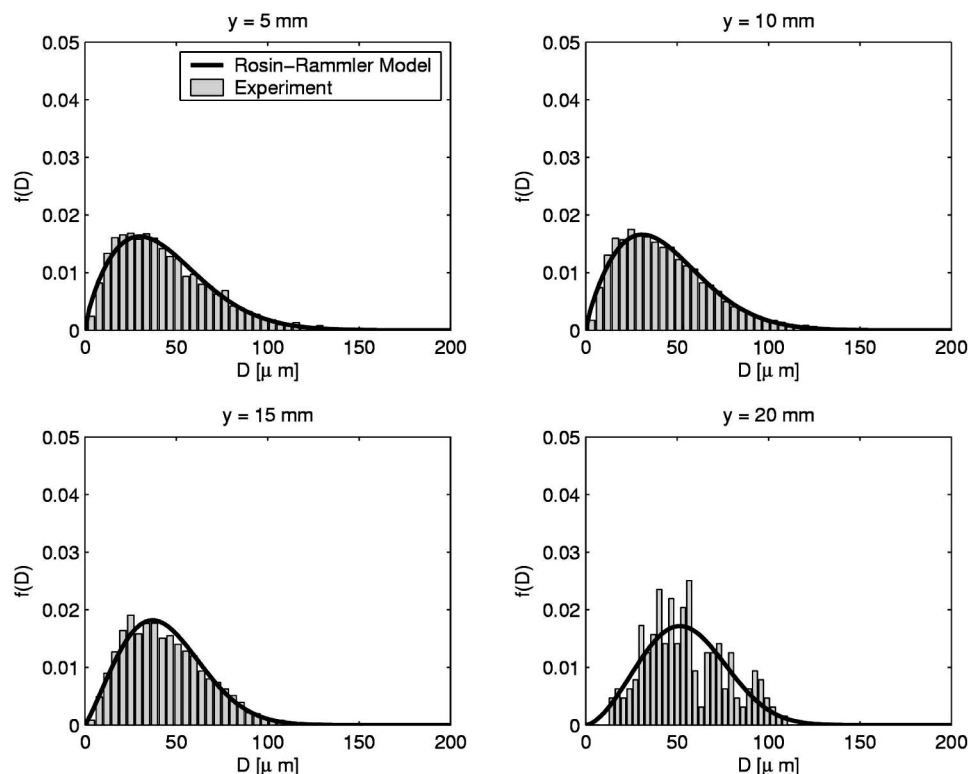


FIG. 13. Experiment of the droplet-size distribution at various radial locations (i.e., $y=5, 10, 15,$ and 20 mm) at the axial location of $x=48$ mm for the $We=87\,193$ case.

location, the droplets are well segregated. Clearly, momentum transfer occurs during this event since small droplets of high velocity merge and release their energy to the dominant convective mainstream; the small droplets of low velocity have the opposite effect. As shown in Fig. 14(b), the small droplets of high velocity mostly have disappeared, which indicates that the small droplets of liquid core are entrained toward the center and their momentum are equalized with the neighbor smaller droplets near the center line.

In Fig. 16(a), the droplet gradation is depicted. The external spray simulation, discussed in Sec. VI C, also confirms the droplet gradation phenomenon as briefly demonstrated in Fig. 16(b); small droplets are entrained toward the center. In Fig. 17(a), the vector plot of air flow is shown. The entrainment near the nozzle exit is clearly simulated. The flow relaxes as the axial location increases, while adjusting their momentum with surrounding air. This flow relaxation at various axial locations is shown in Fig. 17(b).

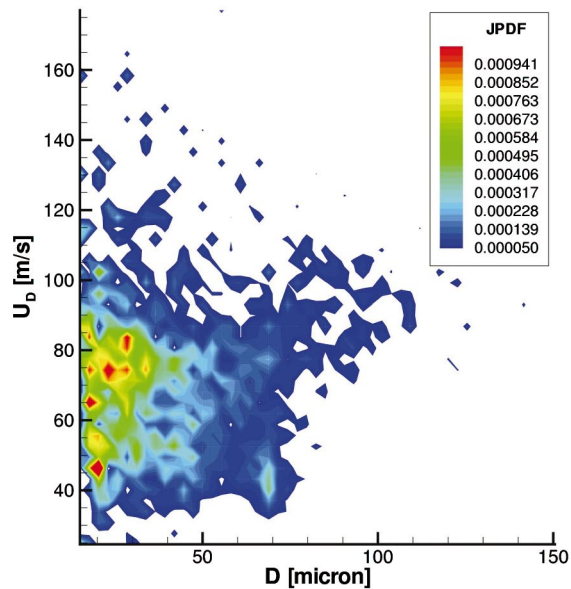
C. External spray simulations using NT distribution

In the preceding Sec. VI A, the NT distribution model is shown to be the model that best describes the droplet size distribution of the liquid core. An important droplet flow physics, droplet gradation, also is identified in Sec. VI B when comparing our computational results at the liquid core and the experimental results at the downstream location $x/d=24$. In this section, the NT distribution is applied as the initial conditions for the droplet size distribution to the stochastic separated flow (SSF) model.³ Our goal in this section is to simulate droplet gradation, flow physics using the NT model as the initial droplet size distribution.

The SSF model has been extended to handle the dilute

multiphase flow physics found in evaporating and reacting sprays.³ The spray model is coupled with the Navier–Stokes solver, based on a Reynolds averaged Navier–Stokes (RANS) formulation employing a standard $k-\epsilon$ turbulence closure model.⁴⁴ The gas-phase flow is calculated on an Eulerian staggered Cartesian grid using the SIMPLEC method.⁴⁵ The condensed phase evolves using a Lagrangian approach based on the stochastic separated flow model.^{43,46} Evolution equations for collections of droplets with similar sizes and initial conditions, denoted as parcels, are used to reduce computational cost. A sufficient number of parcels are used to ensure adequate resolution of the spray physics and the measured droplet statistics.² Statistical variations in droplet size and velocity are imposed as initial conditions to simulate the liquid jet breakup process, of which phenomenon was experimentally shown by Sallam *et al.*^{47,48} In addition, the modified collision/coalescence model of O’Rourke¹⁷ as well as the evaporation model of Ranz and Marshall were used.^{49,50} The parcels are advanced under the influence of modeled turbulent fluctuations in the gas-phase properties.⁵¹

All simulations run for a duration of 2 seconds on $1.2\text{ m} \times 0.8\text{ m} \times 0.8\text{ m}$ domain: $0\text{ m} < x < 1.2\text{ m}$, $-0.4\text{ m} < y < 0.4\text{ m}$, and $-0.4\text{ m} < z < 0.4\text{ m}$. The spray injection is initiated at origin, $x=y=z=0$. A $70 \times 50 \times 50$ Cartesian grid is employed (thus, total numbers of the computational nodes are 175 000) with grid stretching employed to enhance the resolution around the injector location. The flow is essentially steady after $t=0.5$ s and statistics are collected from $t=0.5$ to 2.0 s at intervals of 0.0002 s thus 7500 statistic collection frequency is applied during 1.5 s. Parcels are injected at a rate of 133 333 per second; the average mass associated



(a) Computational result at liquid core

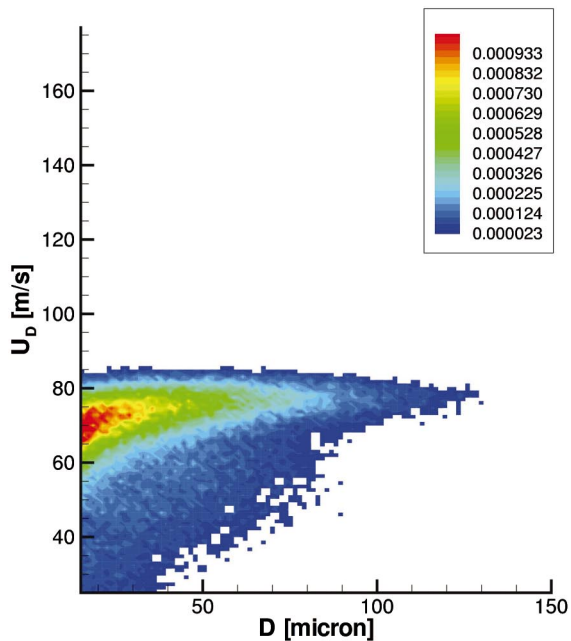
(b) Experimental result at $x = 48$ mm

FIG. 14. (Color). Joint PDFs for the droplet size and velocity for the $We = 87\,193$ case. (a) Computational result at liquid core. (b) Experimental result at $x = 48$ mm for all radial locations.

with each parcel is approximately 1.875×10^{-6} kg of water. Thus, the number of droplets per parcel is approximately $PPP \approx 5.6 \times 10^4$. Constant pressure boundary condition is applied at all boundaries. The nozzle operating pressure is $\Delta p = 4.14$ MPa, which gives the Bernoulli jet speed of $U_{BE} = 91$ m/s. Due to the pressure drop within the internal nozzle flow, the actual jet speed is estimated to be about $U_{inj} = 80$ m/s based on the measured mass flow rate, $\dot{m} = 0.25$ kg/s, and the nozzle diameter, $d = 2$ mm. The droplet injection speed is set as 10.1% less (i.e., $U_{D,inj} = 71.9$ m/s) than the jet speed per BEM prediction in Sec. VI A. The fluctuating droplet injection speed is set as $U_{D,rms}/U_D$

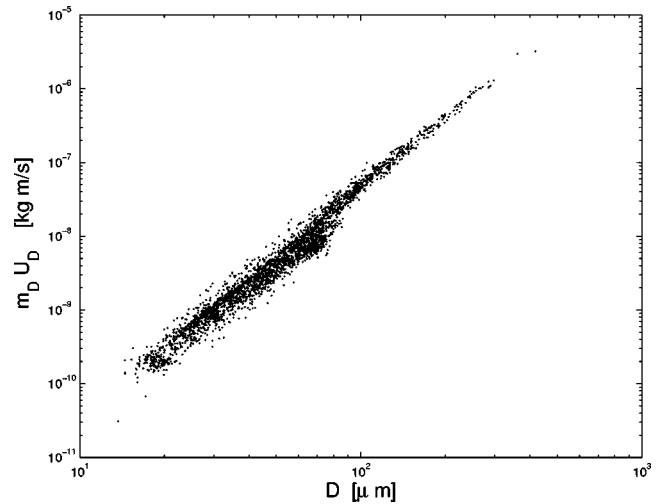


FIG. 15. The initial droplet size vs its momentum at the liquid core. Larger droplets generally have greater momentum. Linear relationship between D and $(m_D U_D)$ is shown.

$= 0.296$ per BEM prediction (see the case $We = 87\,193$ in Table III). The cone angle is set as $\theta = 15^\circ$, based on the experimental observation. The arithmetic mean diameter used as the initial condition during injection is $D_{10} = 39.97$ μm , whose value is predicted by the BEM liquid core model in Sec. VI A (see Fig. 9). Coefficients of the NT distribution are adjusted to best match the droplet size distribution previously identified against the BEM result as in Fig. 12(a). The dimensionless parameters are $Re = U_{inj} d / \nu = 142\,857$, $We = \rho U_{inj}^2 d / \sigma = 174\,387$, $We_g = \rho_g U_{inj}^2 d / \sigma = 215$, and $Oh = \sqrt{We/Re} \approx 0.0023$.

Usually, it is impossible to track all individual droplets and, thus, the SSF model is constructed and used on the basis of the parcel (or cloud) model; one parcel carrying thousands of droplets. In order for conservation equations describing these parcels to accurately represent the evolution of all parcels, droplets in a parcel generally are restricted to a fixed diameter. If the number of droplets in each parcel is identical, then the size distribution of the parcel follows the size distribution droplets. However, it is computationally more expedient to force the mass of each parcel to be identical. Thus, the number of droplets per parcel is inversely proportional to the droplet mass. Equivalently, the number of droplets per parcel is proportional to D^{-3} , where D is the diameter of the droplet. In this case, the parcel distribution, $f_c(D)$, differs from the droplet distribution, $f(D)$,

$$f_c(D) = A_n D^3 f(D), \quad (23)$$

where A_n is a scaling factor so that $f_c(D)$ can be properly normalized. Using Eq. (23), the PDF for the parcel is written as

$$f_c(D) = A_n D^3 a D^p \exp(-b D^c). \quad (24)$$

Here, A_n can be evaluated using the normalization definition, $1 = \int_0^\infty f_c(D) dD$. Thus,

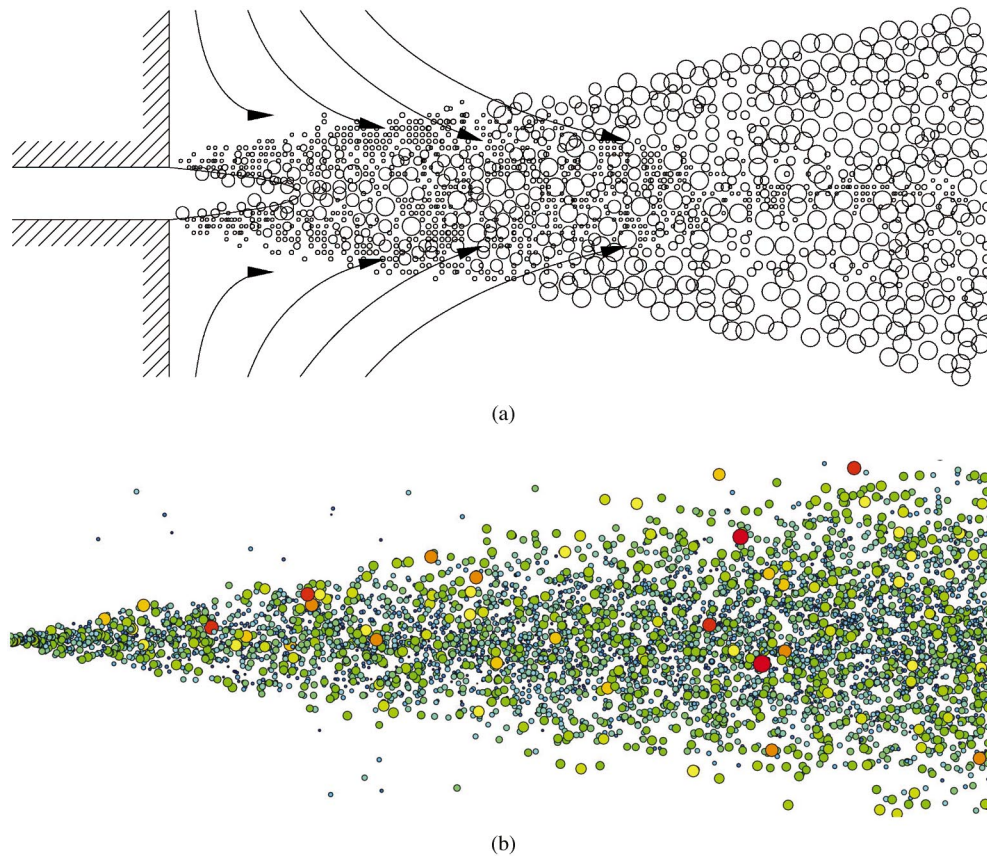


FIG. 16. (Color). (a) Schematic of near field entrainment and droplet size distribution. (b) Cross-sectional view (at $z=0$ plane) of the spray using Nukiyama-Tanasawa distribution as initial conditions. Contour color is scaled with the droplet size; red for large and blue for small droplets. Droplet gradation is shown. As a result, the droplet size increases outwardly (proportional to increasing radial direction). Note that the focused simulation domain extends from $x=0$ to $x=1$ m.

$$A_n = \frac{cb^{p+4}}{a\Gamma\left(\frac{p+4}{c}\right)}. \quad (25)$$

In stochastic simulations, the droplet diameters are obtained by randomly sampling from the cumulative distribution function. The cumulative distribution function corresponding to Eq. (24) is

$$\text{CDF} = \int_0^D f_c(D)dD = 1 - P\left[\frac{p+4}{c}, bD^c\right], \quad (26)$$

where P is known as the incomplete gamma function.⁵² To obtain the parcel size, D , for a specific parcel, the inverse of Eq. (26) is taken,

$$D = \left\{ \frac{1}{b} P^{-1}\left[\frac{p+4}{c}, 1 - \text{CDF}\right] \right\}^{1/c}. \quad (27)$$

In Fig. 18, it is clear that the droplet and the parcel distributions are different. The parcel PDF is shifted to the right because of the larger size distribution of the D^3 effect of Eq. (23). To ensure consistency of Eqs. (24) and (27), the convergence check per droplet number density is performed using various number resolutions as shown in Fig. 19. Using Eq. (27), the parcel size is determined for specific numbers resolution, N , and these parcels are categorized into 35 his-

tograms (or bins). These histograms are compared with the analytical parcel PDF of Eq. (24). It is shown that $N > 1 \times 10^4$ yields a statistically reliable PDF distribution. All simulation results are obtained under the droplet number resolution of $N > 1 \times 10^5$ parcels, which guarantees the solution independence from the number resolution, N .

In Fig. 20, the computational results using the NT distribution are shown and compared with the experimental data at various axial locations (i.e., $x=250, 480,$ and 810 mm). Parameters used for the NT distribution are $p=5, c=1,$ and $b=0.22,$ corresponding to Fig. 12(a). The comparison is poor because the NT distribution using the parameters do not account for distribution of the larger droplets [see Fig. 21, a magnified view of the lower-right region of Fig. 12(a)]. While the NT distribution well describes the high “peak” distribution of the small droplets, the NT model poorly describes the distribution of larger droplets. When the NT parameters are adjusted so that the NT distribution is in agreement with the histograms provided by the liquid core model especially in the lower-right region, the parameters are found as $p=2, c=1,$ and $b=0.08$ (see Fig. 21). Unfortunately, these modified parameters do not well describe the high “peak” of the smaller droplets. It is interesting that modified distribution seems to be in agreement with the log-normal distribution in the lower-right region.

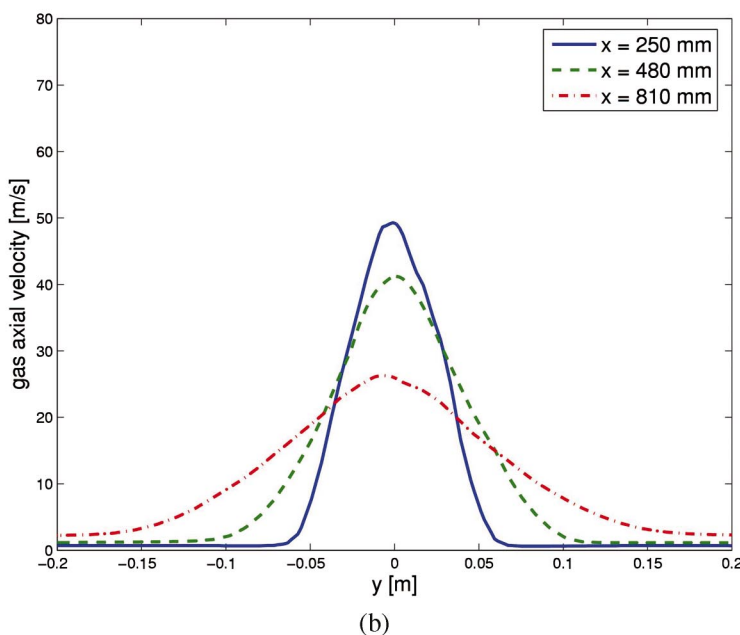
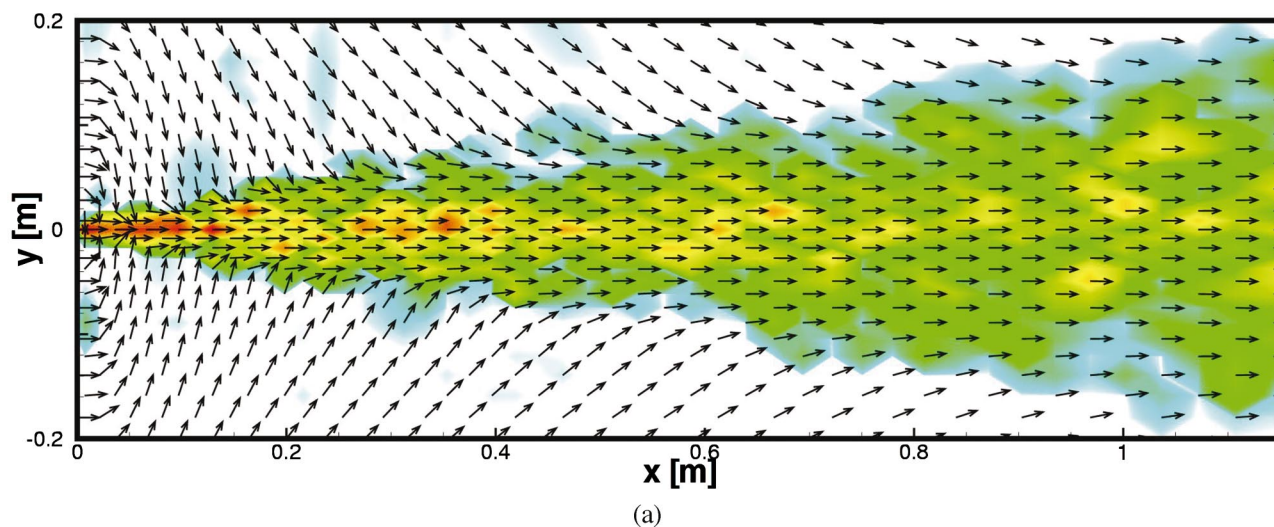


FIG. 17. (Color). (a) Cross-sectional view at $z=0$ plane. Entrainment creates strong inflow near droplet-injection location. As a result, small droplets are convected toward the center line. The contour color is scaled with the droplet number density. (b) Relaxation of the gas axial velocity at various axial locations (i.e., $x=250, 480,$ and 810 mm) is shown.

Since the log-normal distribution well describes the large droplet-size distribution (similar to the modified NT parameters), the log-normal model is of good use for initial conditions as well. The same principle for the parcel injection method is applied to the log-normal distribution as is in the NT distribution of Eqs. (23)–(27). The parcel PDF of the log-normal distribution is written as follows:

$$f_c(D) = D^3 \exp\left(-3 \ln D_{ln} - \frac{9}{2} \sigma_{ln}^2\right) \frac{1}{\sqrt{2\pi} \sigma_{ln} D} \times \exp\left(-\frac{(\ln D - \ln D_{ln})^2}{2\sigma_{ln}^2}\right), \quad (28)$$

where σ_{ln} is the dimensionless standard deviation of the logarithm of the diameter. $D_{ln} = \exp(\ln D)$ is the log-normal diameter defined as the exponent of an average of the logarithm. Kuo and Corsin³⁹ provide the relation between D_{ln} and the average diameter, D_{10} (i.e., $D_{ln} = D_{10} / \exp[\sigma_{ln}^2/2]$).

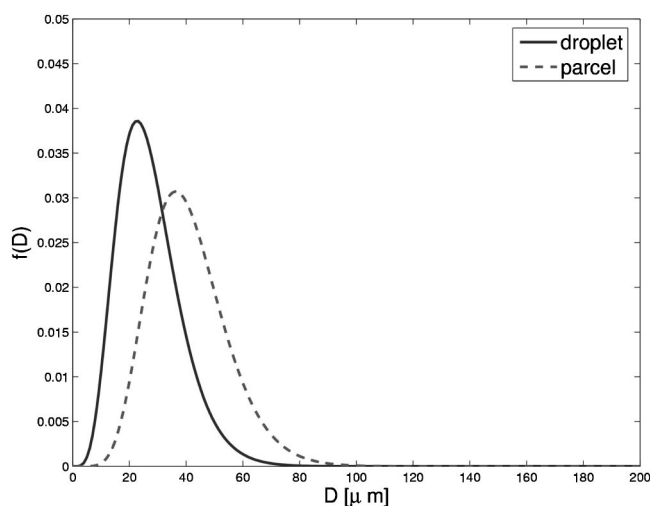


FIG. 18. Comparison between the droplet and parcel distributions for the Nukiyama–Tanasawa PDF. Note $p=5, c=1,$ and $b=0.22$ are used.

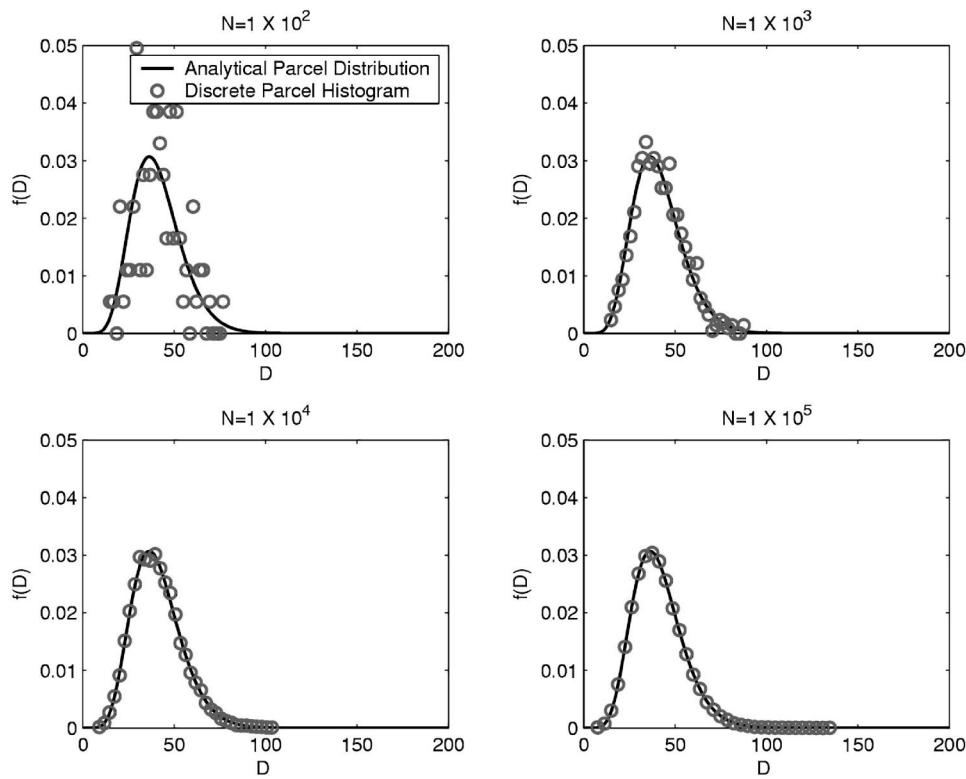


FIG. 19. Droplet number density resolution check for the parcel distribution of the Nukiyama-Tanasawa PDF. Note $p=5$, $c=1$, and $b=0.22$ are used.

Since cumulative distribution function (CDF) is defined as the integral of $f_c(D)$ over the droplet diameter, the parcel diameter can be written as

$$D = D_{in} \exp[\sqrt{2}\sigma_{in} \operatorname{erf}^{-1}(2 \operatorname{CDF} - 1) + 3\sigma_{in}^2]. \quad (29)$$

Here erf^{-1} is the inverse-error function, obtained using the inverse of the incomplete gamma function. For example, $\operatorname{erf}^{-1}(x) = P^{-1}(1/2, x^2)$.

Computational results using Eq. (29) as the initial condition are shown and compared with the experimental data in

Fig. 22. The computational results improved (compared with the results shown in Fig. 20) because the log-normal distribution accounted well for the large droplets, as discussed previously. Both computational and experimental results show, in Fig. 22, that the arithmetic mean diameter increases as the radial location increases. This pattern correctly confirms the droplet gradation phenomenon previously shown and validated in Sec. VI B. The stiffness (i.e., $\Delta D_{10}/\Delta y$) of this gradation behavior becomes less prominent when the axial location increases. A major difference between the computational results and experiment is shown near the center line region (i.e., $y=0$). At a far downstream location x

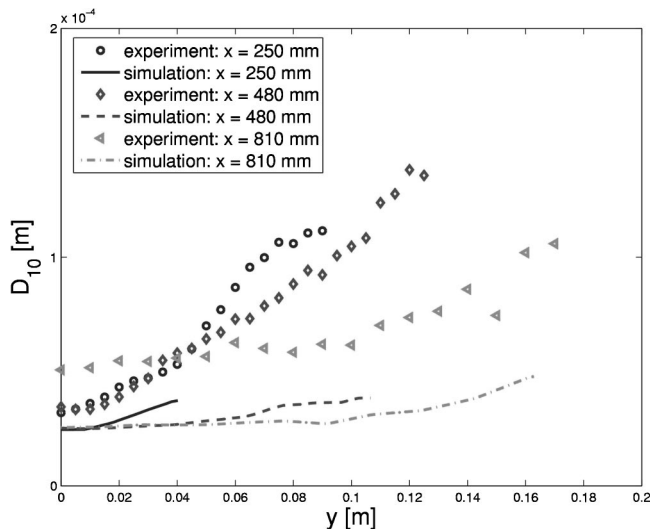


FIG. 20. Nukiyama-Tanasawa parameters (i.e., $p=5$, $c=1$, and $b=0.22$) describe the high “peak” of the smaller droplet size distribution. Poor comparisons are shown when larger droplet size distribution is ignored during the initial droplet injection.

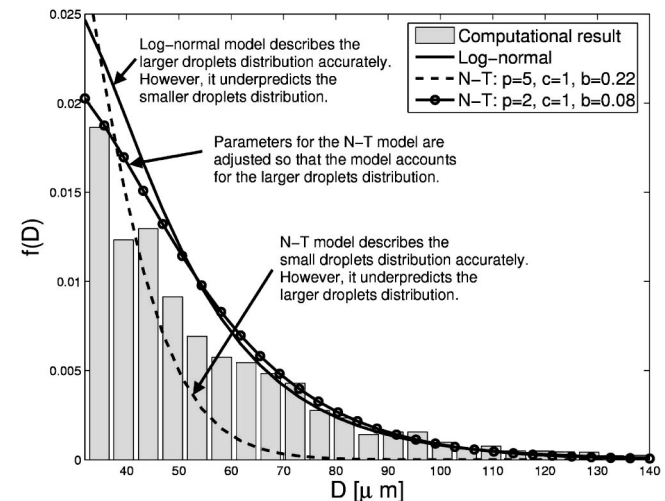


FIG. 21. Magnified view of Fig. 12(a) (lower-right region). Comparison between the Nukiyama-Tanasawa and the log-normal distributions.

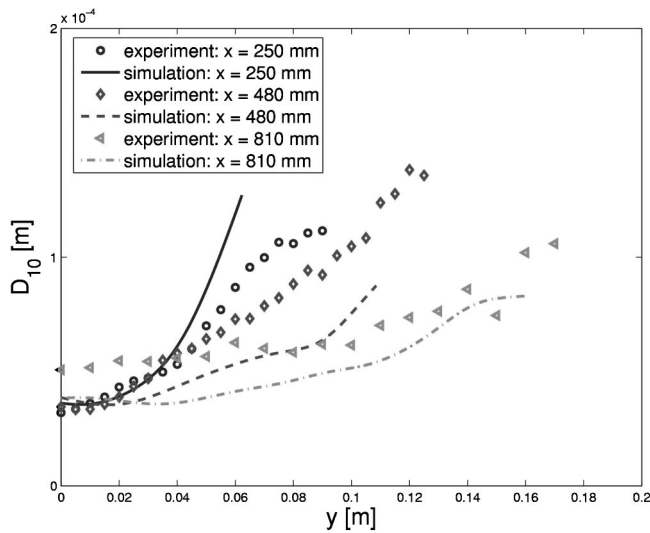


FIG. 22. Arithmetic mean diameter results at various axial locations using the log-normal distribution with $\sigma_{\ln}^* = 0.5$. Comparison improved (compared to that in Fig. 20) because the log-normal takes into account for the larger droplet distribution more accurately.

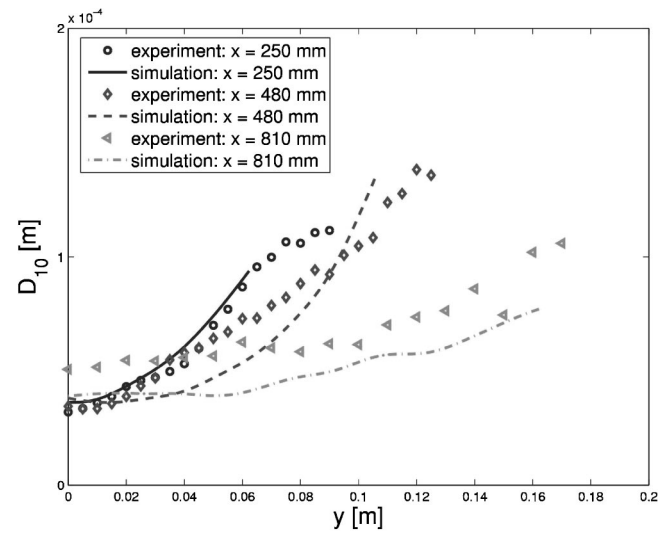


FIG. 23. Arithmetic mean diameter results using $p=2$, $c=1$, and $b=0.08$, Nukiyama-Tanasawa parameters which describes the larger droplet size distribution. Comparison improved (compared to that in Fig. 22) because the NT distribution (with $p=2$, $c=1$, and $b=0.08$) better describe the smaller droplets distribution as well as larger droplets distribution.

=810 mm, the small droplets generally are not carried due to their loss of momentum. In reality, drag plays a significant role in reducing the droplet velocity. In addition, local turbulent eddies arising between the shear layers of the moving droplets and surrounding air cause the jet to diverge substantially. Generally, the stochastic separated flow (SSF) model using the parcels' distribution tends to overpredict droplet momentum because of parcel or cloud modeling. For this reason, small droplets of computation are carried a further distance and, thus, the overall D_{10} results are smaller at $x=810$ mm compared to the experimental data.

In Fig. 23, the computational results again are improved when the NT distribution is used with the modified parameters $p=2$, $c=1$, and $b=0.08$. It is reminded that the NT distribution with the modified parameters better describes the large droplet distribution (see Fig. 21). This comparison suggests that accounting for large droplets is more important than accounting for small droplets when simulating droplet gradation. It is probably because the larger droplets tend to lead the droplet dynamics mechanism during the droplet gradation process. On the other hand, the importance of the

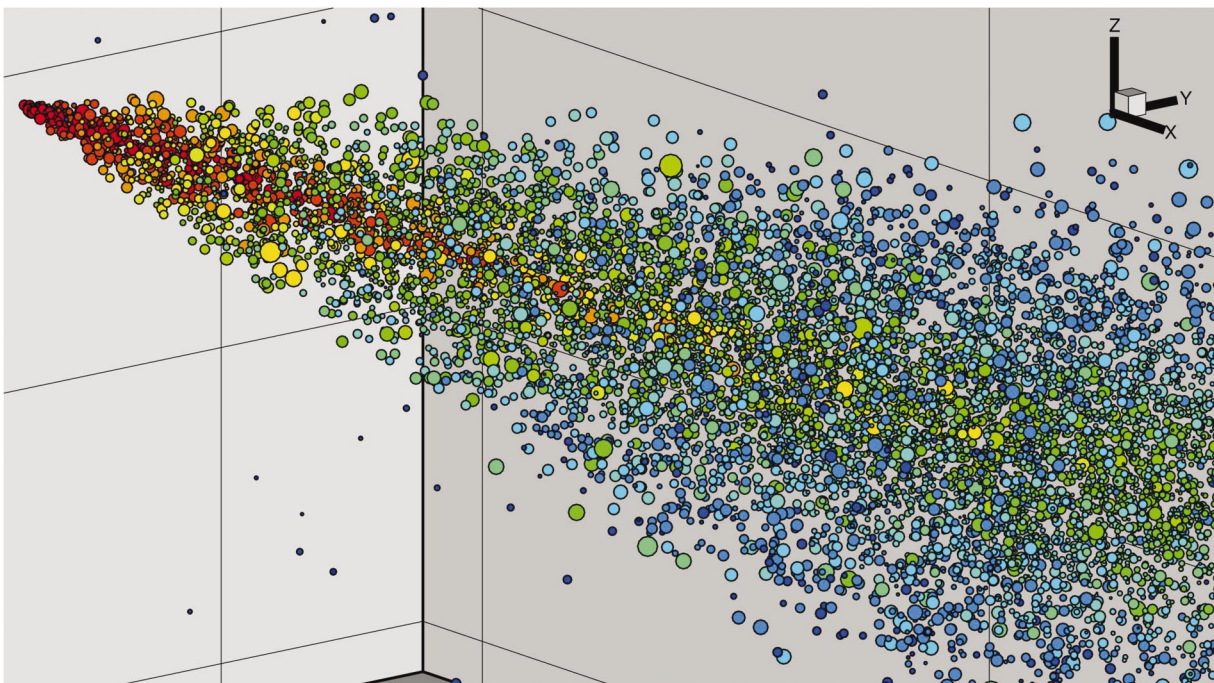


FIG. 24. (Color). A snapshot of a spray. Contour color is scaled with the droplet axial velocity. The velocity is higher closer to the nozzle exit and toward the center line.

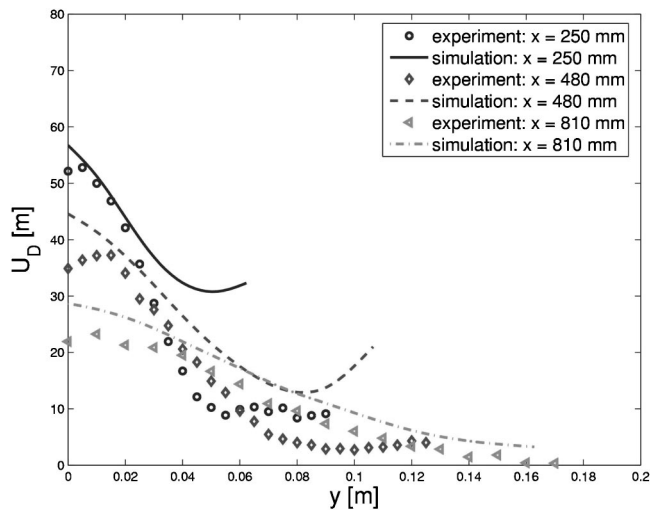


FIG. 25. Average droplet axial velocity results comparison between experiment and simulation.

small droplets should not be underestimated. When the log-normal distribution underestimated the portion of small droplet, as in Fig. 7(d), the droplet size variation in the radial direction ($\Delta D_{10}/\Delta y$) are not properly simulated in Fig. 22. It is observed that more coalescence events occur with the log-normal injection because of greater numbers of larger droplets. Thus, the computational results tend to overshoot the mean droplet size at the $x=250$ mm downstream location as seen in Fig. 22. Thus, the NT distribution with the modified

parameters, which properly accounts for the distributions of both small and large droplets, yields the best computational results.

In Fig. 24, a snapshot of the moving droplets is shown. The droplet velocity is high near the nozzle exit. The droplet velocity is reduced as the droplet travels downstream. It is also shown that droplets located at a larger radius tend to have a smaller velocity due to their greater exposure to air drag. Quantitative comparisons between our computational result and experimental data at various axial locations are shown in Fig. 25. As expected, the droplet velocity is reduced as both axial and radial locations increase. The computational results tend to overpredict droplet velocity because of the nature of the SSF model (discussed previously). The “tailing” behavior of the droplet velocity (shown in Fig. 25 at $x=250$ and 480 mm) is attributed to the greater momentum of the coalesced large droplets upstream.²

VII. EFFECT OF PULSING INJECTION

It is well known that turbulence or/and cavitation causes random fluctuation within the internal nozzle flow. This fluctuation becomes more prominent when the roughness of the pipe inner surface becomes large. During the liquid injection, jet pulsation is imposed to study the random fluctuation effect on the atomizing liquid core and its subsequent effect on droplet characteristics. Here, the pulsation magnitude varies to account for the magnitude of the turbulence fluctuation. These identified droplet characteristics produced during pulsation are used as initial conditions for the SSF model for the

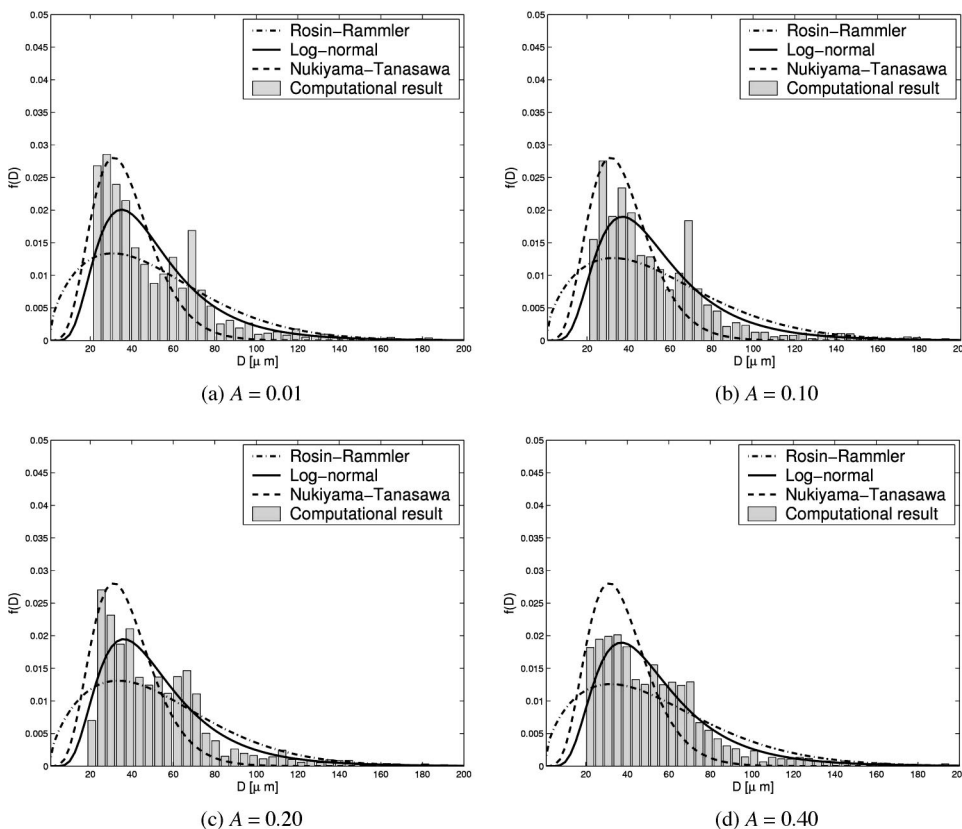


FIG. 26. Simulations of the droplet size distribution at various pulsing magnitude for the $We=10\,000$. (a) $A=0.01$, (b) $A=0.10$, (c) $A=0.20$, (d) $A=0.40$.

TABLE IV. Cases run under different pulsing conditions. Note that nozzle diameter is $d=2$ mm.

Cases	1	4	5	6
We	10 000	10 000	10 000	10 000
A	0.01	0.10	0.20	0.40
U (m/s)	27.02	27.02	27.02	27.02
\bar{U}_D (m/s)	23.32	23.87	25.35	27.24
$\Delta U_{\text{jet} \rightarrow D}$ (%)	13.69	11.66	6.18	0.81
$U_{D,\text{rms}}$ (m/s)	7.19	7.37	8.34	8.82
D_{10} (μm)	50.89	53.93	52.58	54.34
$D_{10,\text{rms}}$ (μm)	28.49	30.92	29.25	30.54
D_{32} (μm)	89.06	97.76	92.39	96.13
q	1.611	1.545	1.603	1.580
N_{drop}	66 222	62 021	73 032	79 761

external spray simulation. The pulsation frequency or wavelength of Eq. (12) also varies to simulate its effect on the overall droplet distribution of the external spray. The most dominant wavelength of the boundary layer instability of Brennen²⁸ is first imposed, and then relatively larger wavelengths are used later. The computational results are compared with experimental results in the downstream location, $x=810$ mm.

A. Effect of pulsing magnitude on droplets of liquid core

Droplet size distributions at various pulsing conditions, $A=0.01, 0.10, 0.20,$ and 0.40 for the $We=10\,000$ case are

shown in Fig. 26. While the highest PDF value tends to reduce its height, the distribution width tends to increase with increasing the pulsing magnitude. The PDF eventually conforms reasonably well into the log-normal shape as shown in the case $A=0.40$ in Fig. 26.

As shown in Table IV, there is no significant change in the mean droplet size, while the pulsing magnitude varies. One noticeable behavior is that the droplet velocity tends to grow with increasing the pulsing magnitude. This pattern perhaps is because the pulsing force increases the local circulation, which induces an additional velocity on separating droplets. It is shown in Sec. VI A that the mean droplet velocity generally is lower than the exiting liquid jet (or slug) velocity. However, the mean droplet velocity can be greater than the jet velocity when the pulsation magnitude is sufficiently large. In this case, the pulsation acts as an external forcing source to the injection system.

In Fig. 27, the width of the droplet velocity distribution becomes slightly larger as the highest PDF value is reduced with increasing the pulsing magnitude. Here, the standard deviation for the log-normal distribution also is found to be $\sigma_{\text{ln}} \approx 0.5$. Thus, the log-normal fit using $\sigma_{\text{ln}}=0.5$ for the droplet velocity distribution seems to be applicable not only for the wide range of Weber number, but also for the wide range of pulsing condition at the liquid core.

A snapshot taken at $t^*=5.8$ is shown in Fig. 28 for the pulsing jet. The pulsing wavelength appears on the liquid surface, while the smaller boundary layer waves randomly appear throughout along the surface line. Evolution of the pulsing jets is shown in Fig. 29 for various pulsing magni-

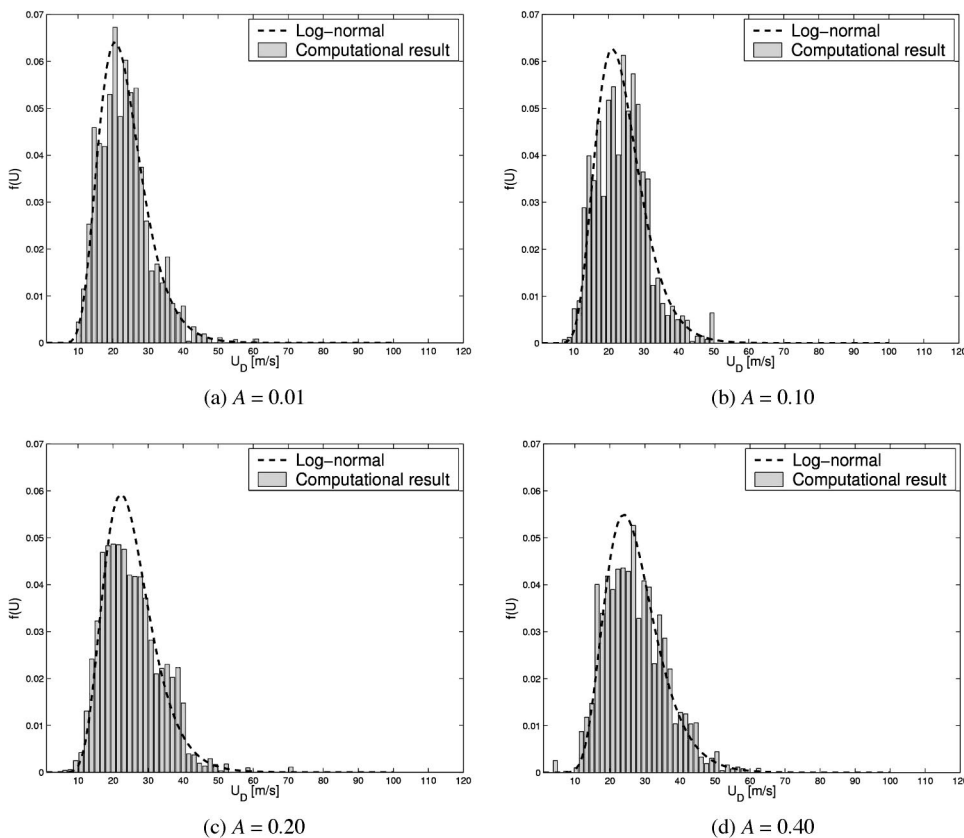


FIG. 27. Simulation of the droplet velocity distribution at various pulsing magnitude for the $We=10\,000$. (a) $A=0.01$, (b) $A=0.10$, (c) $A=0.20$, (d) $A=0.40$.

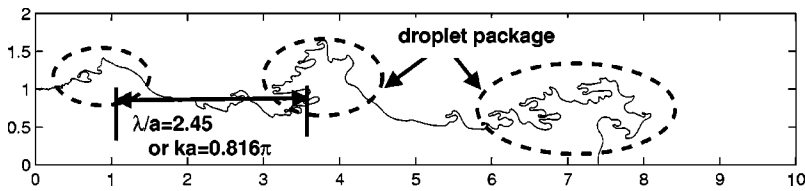


FIG. 28. A snapshot of the pulsing jet simulation in the upper liquid surface is taken at $t^* = 5.8$ for case 5 (i.e., $A = 0.2$). The pulsing frequency or wavelength (i.e., $ka = 0.816\pi$ or $\lambda/a = 2.45$) appears on the liquid surface.

tude. It is shown that the pulsing magnitude should be sufficiently large (i.e., $A \geq 0.10$) for the prominent appearance of the pulsing wavelength on the liquid surface. In Fig. 29, the typical shapes of the liquid core for a turbulent jet are shown (see Fig. 29, the snapshots taken at $t^* = 7.0$). The liquid core is deformed in a chunk-like “droplet-package” at an interval of the pulsing wavelength when the pulsing magnitude is of sufficient magnitude (i.e., $A \geq 0.20$). At relatively high speed, the liquid core of a turbulent jet is extremely difficult to observe because of intense multiple light scattering from surrounding liquid droplets. In Fig. 29, the distorted shape of the liquid core due to the pulsation is clear. However, data collected in Table IV and Figs. 26 and 27 indicate that droplet characteristic variations due to pulsation is relatively insignificant when compared with the droplet characteristics variation due to the Weber number increase (see Sec. VI A). While the pulsation is important enough to affect the droplet characteristics for the low speed jet in the Rayleigh regime,⁵³ it is uncertain whether the pulsation can affect the droplet characteristics for the high speed turbulent jet in the atomization regime. This uncertainty leads us to simulate the external spray under the pulsing injection. We will investigate droplet characteristics at various pulsation wavelengths and will present its sensitivity on the final results in Sec. VII B.

B. Effect of pulsing wavelength on droplet characteristics for external spray

Pulsation droplet statistics of the liquid core, previously identified in Sec. VII A, are used as initial conditions for the SSF model to clarify the uncertainty associated with the pulsation effect for the turbulent jet.

The pulsating magnitude was set as $A = 0.4$, whose value is sufficiently large to guarantee the appearance of the pulsing wavelength. However, no discernable effect is shown during the SSF external spray simulation when the jet is pulsed with the relatively small-scale wave of the turbulent boundary layer ($\lambda = 2.45a$, previously appeared in the liquid core surface as in Fig. 28). Thus, larger wavelengths ($\lambda = 100a$, $200a$, and $300a$) are used during pulsation and their prominent effect on the droplet dynamics is shown in Fig. 30. It is clear that the droplets are well segregated at an interval of the pulsing wavelength. This distinctively segregated conglomeration confirms the existence of the “droplet-package” of the liquid core (shown in Fig. 28) breaking up into a cloud of droplets. It is shown that the conglomerated region becomes obscure as the droplets travel downstream. The triangulated mesh is constructed in Fig. 31 to study the droplet characteristics at a quasisteady state. Figure 32 shows

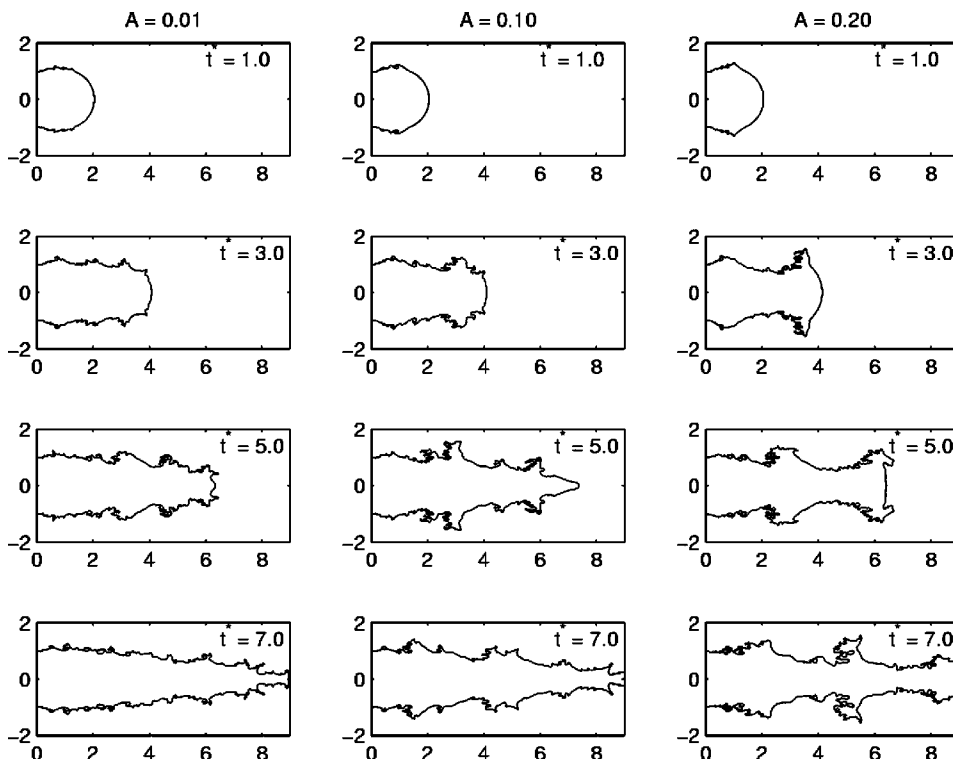


FIG. 29. Evolution of the pulsing jet at various pulsing magnitude, $A = 0.01$, 0.10 , and 0.20 .

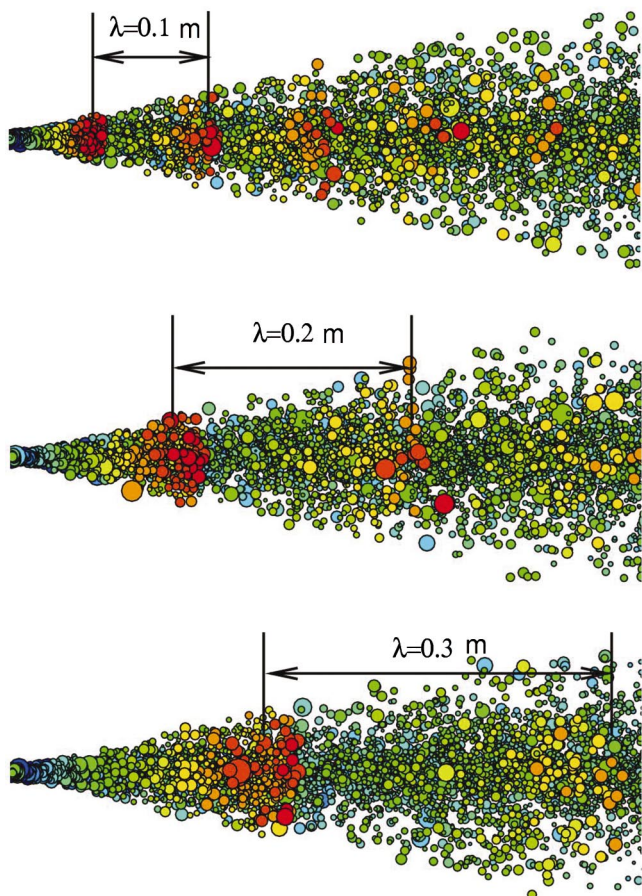


FIG. 30. (Color). Snapshot of the pulsing jet with different pulsing wavelength, $\lambda=0.1, 0.2,$ and 0.3 m. Contour color is scaled with the axial velocity of droplets. Note, the computational domain shown in this figure extends from $x=0$ to $x=0.55$ m. The pulsing magnitude is $A=0.4$.

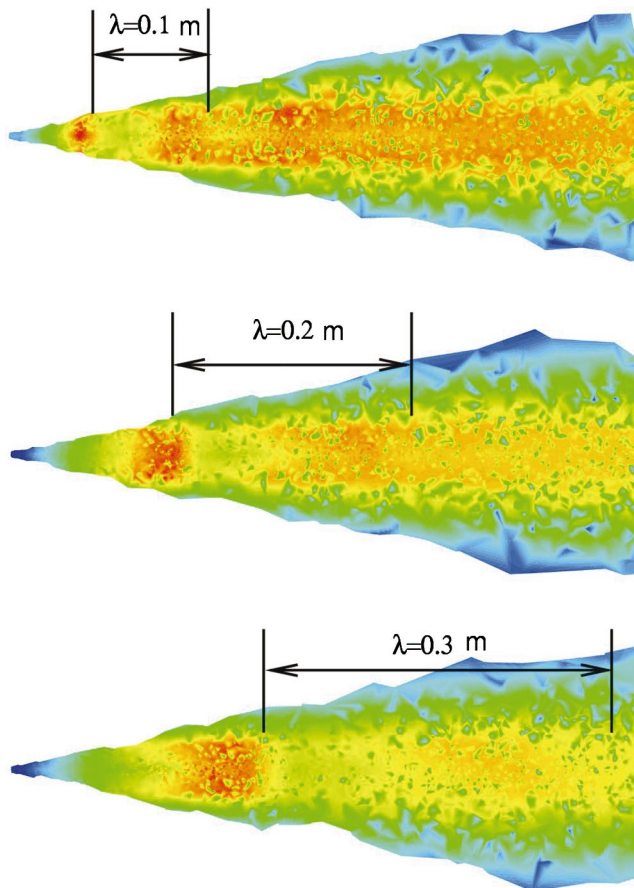


FIG. 32. (Color). A snapshot of the local gas axial velocity corresponding to Fig. 30.

that the local axial velocity of air is affected by the jet pulsation. Obscurity of the pulsation with increasing the downstream location is again confirmed in Fig. 32. A snapshot of the droplet size distribution shown in Fig. 33 indicates that the pulsation essentially has no effect on the overall droplet size distribution as no discernable pulsation effect is shown. A quantitative comparison is made in Fig. 34 at the axial location, $x=810$ mm, using the Eulerian droplet statistics. As shown, the jet pulsation has little effect on the final droplet statistics of its size and velocity.

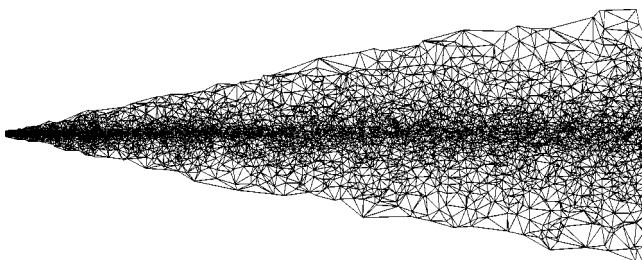


FIG. 31. Triangulated mesh for droplets.

VIII. CONCLUSIONS

A numerical model to obtain droplet characteristics at the liquid core of high velocity turbulent liquid spray is explained and demonstrated. Results are obtained under various Weber numbers and pulsing conditions for fully developed turbulent flows. Some limited experimental data also are presented and compared against computational results. Computational results yielded the following observations:

- (i) Boundary layer instability is solely responsible for characterizing the droplet size distribution at the liquid core for a turbulent liquid spray; no shear-layer driven (i.e., Kelvin–Helmholtz type) instability plays an important role in determining the initial droplet size in the liquid core region. Current state-of-the-art liquid core modeling using BEM with the superposition theory can accurately predict the droplet size and velocity distribution at the liquid core region. No adjustable constant is used for the BEM liquid core model. The secondary instability model can improve by adopting the nonlinear effect (see Fig. 4). A nonlinear model for the secondary instability,³⁸ would address the very small droplet size distribution of the liquid core.
- (ii) The BEM liquid core model predicts an accurate droplet distribution because the analytical PDFs better

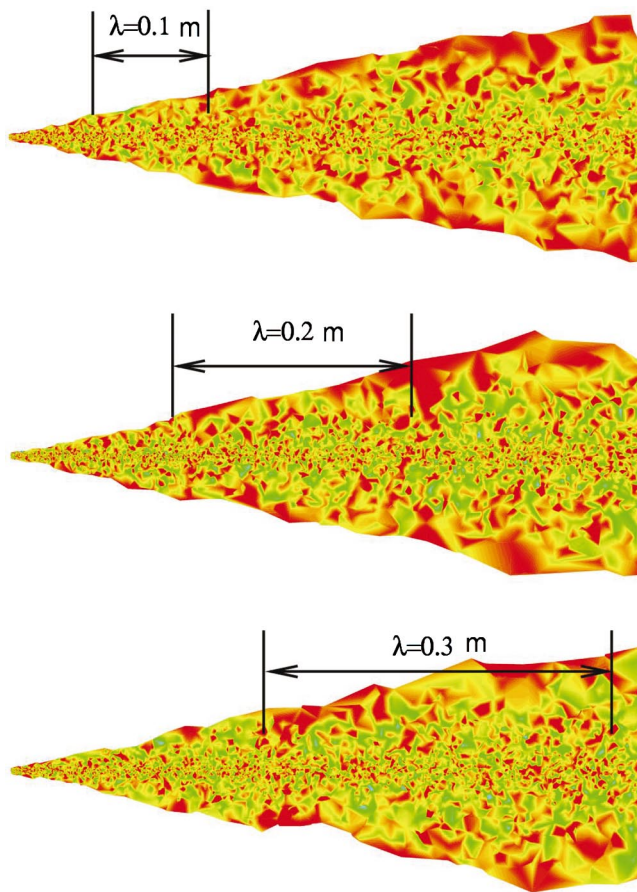
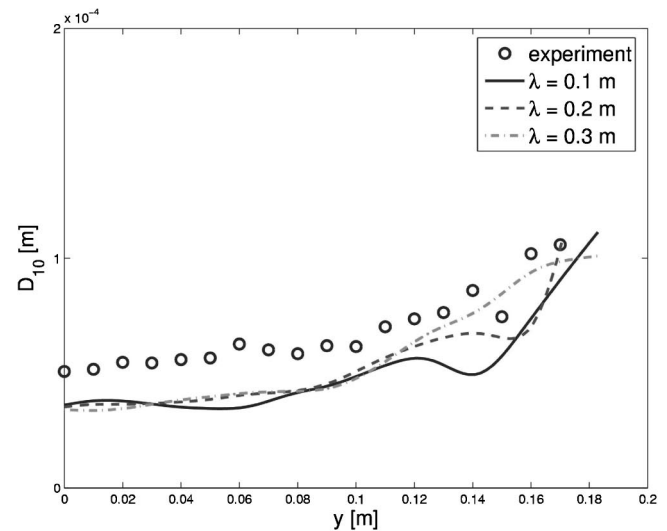


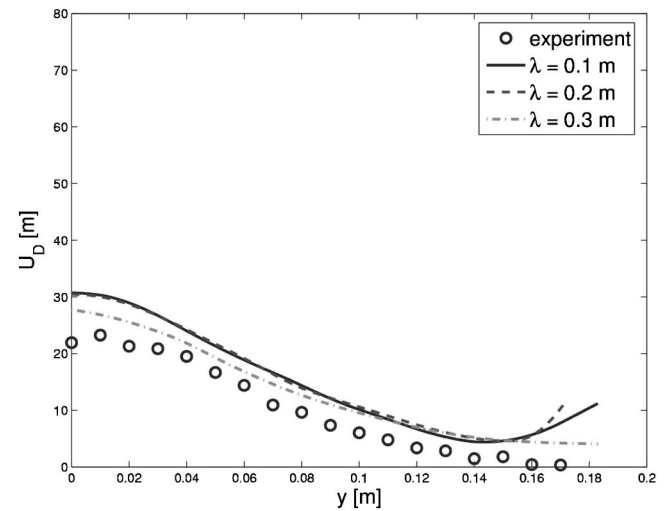
FIG. 33. (Color). Droplet size distributions for various pulsing conditions correspond to Fig. 30. Contour color is scaled with the droplet size. Larger droplet at larger radius is shown while no discernable pulsation effect is observed.

match with the BEM predictions yielding the best comparisons with the experimental data.

- (iii) Extrapolating D_{10} using experimental data in downstream is a suitable method for estimating the initial droplet size at the liquid core. These extrapolated experimental data are in agreement with the prediction of our liquid core model within a 2% error rate.
- (iv) The NT PDF model can effectively describe droplet size distribution in the liquid core region with appropriate adjustable constants (see Fig. 35 for a summary).
- (v) The log-normal PDF model effectively can describe both droplet size and velocity distributions in the liquid core region. However, the model has a shortcoming in describing the small droplet distribution. The dimensionless standard deviation of the log-normal distribution of $\sigma_{ln}=0.5$ seems to be universally applicable for a wide range of droplet sizes and velocities (see Fig. 35 for a summary).
- (vi) Describing larger droplet distribution at the liquid core is critical as the dominant mechanism of the droplet dynamics is essentially governed by larger droplets. At the same time, the importance of the small droplet distribution should not be underestimated as lacking small droplet distribution underesti-



(a)



(b)

FIG. 34. Quantitative comparisons between experiment and simulation results for various injection wavelengths. The log-normal distribution is used for the pulsing injection with the pulsing magnitude, $A=0.4$. (a) Arithmetic mean diameter is compared. (b) Average axial velocity of droplet is compared.

mates the coalescence events and significance of the evaporation.

- (vii) Parcel or cloud distribution for the stochastic separated flow model for both the NT and the log-normal distributions are newly developed and used for the simulation.
- (viii) Droplet gradation occurs immediately after the droplet separation from the liquid core. At a certain downstream location, the Rosin–Rammler PDF model can describe both droplet size and velocity distribution effectively (see Figs. 11 and 13).
- (ix) The droplet gradation phenomenon of the turbulent spray is favored in the fire suppression application. Larger droplets enveloping smaller droplets yield a deep penetration of the spray into fire due to the greater momentum of the larger droplets, while the

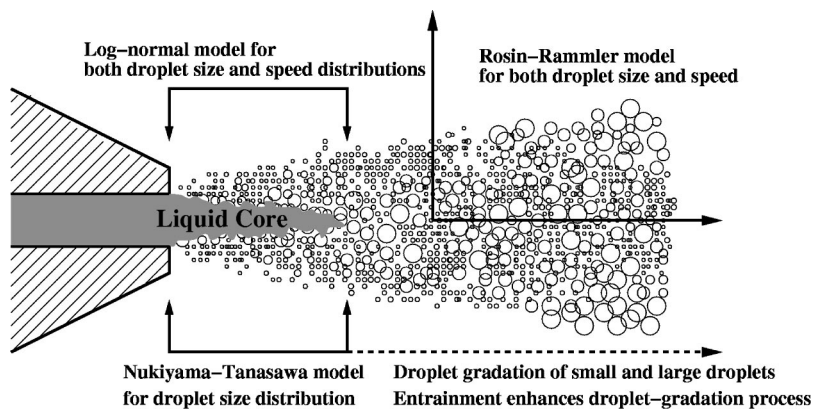


FIG. 35. Summaries of the applicability of analytical distribution models at various physical locations.

smaller droplets can quickly evaporate once they are carried into the fire core.

- (x) It is found that the droplet-number density is proportional to the jet velocity.
- (xi) The droplet velocity is generally from 10%–15% smaller than the exiting jet velocity.
- (xii) Since the droplet size distribution is related to the droplet velocity distribution as shown in Fig. 14, the joint PDF injection method³⁴ is suggested for another possible improved injection method.
- (xiii) Pulsation effect on droplet characteristics is relatively small though increasing pulsing magnitude causes a slightly more dispersive behavior in both size and velocity PDFs.
- (xiv) Pulsation effects (both magnitude and wavelength) are prominent near the liquid core region. In addition, it is found that pulsation tends to increase droplet velocity during launching from the liquid core. However, the overall effects are greatly obscured by the droplet-gradation phenomenon.

A physical process of the droplet shedding to dispersion from the liquid core clearly is shown in our simulation. This enabled an improved understanding of the atomization process in a liquid jet in the liquid core region. Moreover, ideal distribution models for droplet size and velocity at the liquid core region are identified and, therefore, the modeled PDFs are recommended for spray dynamicists to use the PDFs as initial conditions. A fully coupled simulation for an entire spray, combining both internal and external flows, is demonstrated, and its computational results are compared with the experimental data. The comparison is in good agreement.

ACKNOWLEDGMENT

Sandia National Laboratories is a multiprogram laboratory operated by Sandia Corporation, a Lockheed Martin Company for the United States Department of Energy's National Nuclear Security Administration under Contract No. DE-AC04-94AL85000.

¹S. Nukiyama and E. Tanasawa, "Experiments on the atomization of liquids in an air stream," *Trans. Jpn. Soc. Mech. Eng.* **5**, 62 (1939).

²S. S. Yoon, J. C. Hewson, P. E. DesJardin, D. J. Glaze, A. R. Black, and R. R. Skaggs, "Numerical modeling and experimental measurements of a high-velocity solid-cone water spray for use in fire suppression applica-

tion," *Int. J. Multiphase Flow* **30**, 1369 (2004).

³P. E. DesJardin and L. A. Gritzo, "A dilute spray model for fire simulations: Formulation, usage and benchmark problems," Sandia National Laboratories Technical Report No. SAND2002-3419, Albuquerque, 2002.

⁴E. Babinsky and P. E. Sojka, "Modeling drop size distributions," *Prog. Energy Combust. Sci.* **28**, 303 (2002).

⁵E. L. Crow and K. Shimizu, *Lognormal Distributions: Theory and Applications* (Marcel Dekker, New York, 1988).

⁶J. Ponstein, "Instability of rotating cylindrical jets," *Appl. Sci. Res., Sect. A* **8**, 425 (1959).

⁷W. S. Rayleigh, "On the instability of jets," *Proc. London Math. Soc.* **10**, 4 (1878).

⁸C. Weber, "Zum Zerfall eines Flüssigkeitsstrahles," *Z. Angew. Math. Mech.* **11**, 138 (1931).

⁹V. G. Levich, *Physicochemical Hydrodynamics* (Prentice Hall, Englewood Cliffs, NJ, 1962), pp. 639–646.

¹⁰A. M. Sterling and C. A. Sleicher, "The instability of capillary jets," *J. Fluid Mech.* **68**, 477 (1975).

¹¹R. D. Reitz and F. V. Bracco, "Mechanism of atomization of a liquid jet," *Phys. Fluids* **25**, 1730 (1982).

¹²X. Li, L. P. Chin, R. S. Tankin, T. Jackson, J. Stutrud, and G. Switzer, "Comparison between experiments and predictions based on maximum entropy for sprays from a pressure atomizer," *Combust. Flame* **86**, 73 (1991).

¹³C. W. M. Van Der Geld and H. Vermeer, "Prediction of drop size distributions in sprays using the maximum entropy formalism: The effect of satellite formation," *Int. J. Multiphase Flow* **20**, 363 (1994).

¹⁴J. Cousin, S. J. Yoon, and C. Dumouchel, "Coupling of classical linear theory and maximum entropy formalism for prediction of drop size distribution in sprays: Application to pressure-swirl atomizers," *Atomization Sprays* **6**, 601 (1996).

¹⁵S. K. Mitra and X. Li, "A predictive model for droplet size distribution in sprays," *Atomization Sprays* **9**, 29 (1999).

¹⁶J. Cao, "On the theoretical prediction of fuel droplet size distribution in nonreactive diesel sprays," *J. Fluids Eng.* **124**, 182 (2002).

¹⁷P. J. O'Rourke, "Collective drop effects on vaporizing liquid sprays," Ph.D. thesis, Princeton University, 1981.

¹⁸S. S. Yoon and S. D. Heister, "A nonlinear atomization model based on a boundary layer instability mechanism," *Phys. Fluids* **16**, 47 (2004).

¹⁹J. Geiswiler, E. Robert, L. Hure, C. Cachoncinlle, R. Viladrosa, and J. M. Pouvesle, "Flash x-ray radiography of argon jets in ambient air," *Meas. Sci. Technol.* **9**, 1537 (1998).

²⁰E. Robert, L. Hure, C. Cachoncinlle, R. Viladrosa, and J. M. Pouvesle, "Simultaneous flash x-ray induced fluorescence imaging and radiography of argon jets in ambient air," *Meas. Sci. Technol.* **10**, 789 (1999).

²¹C. F. Powell, Y. Yue, R. Poola, and J. Wang, "Time-resolved measurements of supersonic fuel sprays using synchrotron x-rays," *J. Synchrotron Radiat.* **7**, 356 (2000).

²²Y. Yue, C. F. Powell, R. Poola, J. Wang, and J. K. Schaller, "Quantitative measurements of diesel fuel spray characteristics in the near nozzle region using x-ray absorption," *Atomization Sprays* **11**, 471 (2001).

²³A. G. MacPhee, M. W. Tate, C. F. Powell, Y. Yue, M. J. Renzi, A. Ercan, S. Narayanan, E. Fontes, J. Walther, J. Schaller, S. M. Gruner, and J. Wang, "X-ray imaging of shock waves generated by high-pressure fuel sprays," *Science* **295**, 1261 (2002).

²⁴W. Cai, C. F. Powell, Y. Yue, S. Narayanan, J. Wang, M. W. Tate, J. J.

- Renzi, A. Ercan, E. Fontes, and S. M. Gruner, "Quantitative analysis of highly transient fuel sprays by time-resolved x-radiography," *Appl. Phys. Lett.* **83**, 1671 (2003).
- ²⁵H. Park, S. S. Yoon, and S. D. Heister, "A fully nonlinear primary atomization model for high-speed jets," in 16th Annual Conference on Liquid Atomization and Spray Systems, Monterey, CA, 2003.
- ²⁶J. A. Liggett and P. L. F. Liu, *Boundary Integral Equation Method for Porous Media Flow* (George Allen and Unwin, London, 1983).
- ²⁷J. O. Hinze, *Turbulence*, 2nd ed. (McGraw-Hill, New York, 1975), pp. 625–631.
- ²⁸C. Brennen, "Cavity surface wave patterns and general appearance," *J. Fluid Mech.* **44**, 33 (1970).
- ²⁹F. M. White, *Viscous Fluid Flow*, 2nd ed. (McGraw-Hill, New York, 1991), pp. 235, 269, 358.
- ³⁰L. A. Salami, "An investigation of turbulent developing flow at the entrance to a smooth pipe," *Int. J. Heat Fluid Flow* **7**, 247 (1986).
- ³¹J. W. Hoyt and J. J. Taylor, "Turbulence structure in a water jet discharging in air," *Phys. Fluids* **20**, s253 (1977).
- ³²H. Y. Kim, Z. C. Feng, and J. H. Chun, "Instability of a liquid jet emerging from a droplet upon collision with a solid surface," *Phys. Fluids* **12**, 531 (2000).
- ³³S. D. Aziz and S. Chandra, "Impact, recoil and splashing of molten metal droplets," *Int. J. Heat Mass Transfer* **43**, 2841 (2000).
- ³⁴N. Z. Mehdizadeh, S. Chandra, and J. Mostaghimi, "Formation of fingers around the edges of a drop hitting a metal plate with high velocity," *J. Fluid Mech.* **510**, 353 (2004).
- ³⁵K. Range and F. Feuillebois, "Influence of surface roughness on liquid drop impact," *J. Colloid Interface Sci.* **203**, 16 (1998).
- ³⁶W. M. Kays and M. E. Crawford, *Convective Heat and Mass Transfer*, 2nd ed. (McGraw-Hill, New York, 1980), pp. 66–68, 174–176.
- ³⁷M. C. Yuen, "Non-linear capillary instability of a liquid jet," *J. Fluid Mech.* **40**, 495 (1970).
- ³⁸P. Lafrance, "Nonlinear breakup of a liquid jet," *Phys. Fluids* **17**, 1913 (1974).
- ³⁹A. Y. Kuo and S. Corrsin, "Experiments on internal intermittency and fine-structure distribution functions in a fully turbulent fluid," *J. Fluid Mech.* **50**, 285 (1971).
- ⁴⁰A. H. Lefebvre, *Atomization and Sprays* (Taylor and Francis, New York, 1989).
- ⁴¹S. S. Yoon and S. D. Heister, "Categorizing linear theories for atomizing round jets," *Atomization Sprays* **13**, 499 (2003).
- ⁴²P. K. Wu, L. K. Tseng, and G. M. Faeth, "Primary breakup in gas/liquid mixing layers for turbulent liquids," *Atomization Sprays* **2**, 295 (1992).
- ⁴³G. M. Faeth, "Evaporation and combustion of spray," *Prog. Energy Combust. Sci.* **9**, 1 (1983).
- ⁴⁴W. P. Jones and B. E. Launder, "The prediction of laminarization with a two-equation model of turbulence," *Int. J. Heat Mass Transfer* **15**, 301 (1972).
- ⁴⁵S. V. Patankar, *Numerical Heat Transfer and Fluid Flow* (Taylor and Francis, New York, 1980).
- ⁴⁶G. M. Faeth, "Mixing, transport and combustion in sprays," *Prog. Energy Combust. Sci.* **13**, 293 (1987).
- ⁴⁷K. A. Sallam and G. M. Faeth, "Drop formation at the surface of plane turbulent liquids in still gases," *Int. J. Multiphase Flow* **25**, 1161 (1999).
- ⁴⁸K. A. Sallam, Z. Dai, and G. M. Faeth, "Drop formation at the surface of plane turbulent liquid jets in still gases," *Int. J. Multiphase Flow* **28**, 427 (2002).
- ⁴⁹W. E. Ranz and W. R. Marshall, "Evaporation from drops: Part I," *Chem. Eng. Prog.* **48**, 141 (1952).
- ⁵⁰W. E. Ranz and W. R. Marshall, "Evaporation from drops: Part II," *Chem. Eng. Prog.* **48**, 173 (1952).
- ⁵¹J. S. Shuen, L. D. Chen, and G. M. Faeth, "Evaluation of a stochastic model of particle dispersion in a turbulent round jet," *AIChE J.* **29**, 167 (1983).
- ⁵²M. Abramowitz and I. A. Stegun, *Handbook of Mathematical Functions* (Dover, New York, 1970).
- ⁵³C. A. Spangler, J. H. Hilbing, and S. D. Heister, "Nonlinear modeling of jet atomization in the wind-induced regime," *Phys. Fluids* **7**, 964 (1995).
- ⁵⁴W. A. Sirignano, *Fluid Dynamics and Transport of Droplets and Sprays* (Cambridge University Press, Cambridge, 1999).